Delft University of Technology
Master of Science Thesis in Embedded Systems

A New Type Of Medium Access Control For Event Driven Energy Harvesting Devices

Niels Hinderikus Hokke

TU Delft Delft University of Technology

A New Type Of Medium Access Control For Event Driven Energy Harvesting Devices

Master of Science Thesis in Embedded Systems

Embedded and Networked Systems Group
Faculty of Electrical Engineering, Mathematics and Computer Science
Delft University of Technology
Mekelweg 4, 2628 CD Delft, The Netherlands

Niels Hinderikus Hokke
N.H.Hokke@student.tudelft.nl
email@nielshokke.nl
4610148

13-07-2020

Author
Niels Hinderikus Hokke (N.H.Hokke@student.tudelft.nl)(email@nielshokke.nl)
Title
A New Type Of Medium Access Control For Event Driven Energy Harvesting Devices
MSc presentation
15-07-2020

Graduation Committee

Dr. Rango Rao Venkatesha Prasad (direct supervisor)	Delft University of Technology
Dr. Arjan van Genderen	Delft University of Technology
Dr. Qing Wang	Delft University of Technology

Abstract

We present a new ultra low-power MAC protocol for networks of event-driven energy-harvesting devices. We specifically target applications with extremely stringent energy requirements, using devices void of energy buffers that harvest energy from ephemeral events, *e.g.,* a switch, a vibration, or an impact. To cater for this challenging setting, we introduce a new concept of preventing collisions based on RF-harvesting, whereby energy harvested from the radio medium is utilized to infer its occupancy and to break the symmetry between multiple concurrently-transmitting devices. The new concept is instrumental to improve performance in network scenarios demanding immediate transmissions and tiny wake-up times. We build a hardware/software proof of concept implementation of the new mac protocol and concept. We specifically present a protocol model and formulate the mathematical framework to study the performance of a network of event-based harvesting devices following the new MAC. Comparing the new MAC against main contention-based MAC protocols, we show that it outperforms pure Aloha and 1-CSMA by factors of 3.55 and 1.21 respectively in terms of throughput, while it saturates at more than double the offered load compared to 1-CSMA. As traffic increases, the energy savings achieved by by the new MAC against CSMA protocols increase, consuming even 36% less energy than np-CSMA at high offered load showcasing its capability to scale.

Preface

In the summer of 2019, I was asked to join the Zero Heroes, a student team lead by Dr. Rango Rao Venkatesha Prasad (VP). Together with the team we entered the Airbus Fly Your Ideas competition, a global student competition promoting innovation within the aerospace domain. We proposed the idea of an event-driven energy harvesting sensor node which could be integrated throughout the aircraft, *e.g.,* attendant-call buttons, overhead baggage-bins, seat-belt buckles, and storage trays. Reporting to a base station when the encompassing item is used. With this concept we managed to convince the jury and bring home the first price. However, the concept of large numbers of event-driven energy harvesting nodes in a small area, brought up new problems, that limited scalabililty, that were yet unsolved. Due to the extreme energy-constrains, effective medium utilisation becomes impossible using existing solutions, this problem became the topic of my thesis.

I would like to thank my supervisor, VP, for his guidance, and for his suggestion of writing a paper about my solution. I would also like to thank VP, Sujay Narayana, Vijay S. Rao, and especially Nikos Kouvelas for helping writing the paper, of which a large part of the text is re-used in this report.

Furthermore, I would like to thank my family, who supported me throughout the whole journey, especially during the last few months of my thesis, which were made more difficult by COVID-19.

Most importantly, I would like to thank my girlfriend, who despite working on her own thesis, still found the time and energy to support me in writing mine.

Niels Hinderikus Hokke

Delft, The Netherlands

13th July 2020

Contents

Chapter 1

Introduction

Systems of IoT-devices are becoming smarter in all verticals, standing up to the challenge of ubiquitous connectivity in the future Smart Cities and Industry 4.0. To this direction, the unbounded growth of IoT enables a wide range of applications of ever-increasing pervasiveness, as billions of sensors sample the real world; a typical smart factory requires 0.5 IoT-devices per m^2 and a smart city accommodates between 10,000-200,000 devices per km^2, depending on the crowdedness of the area (e.g., business center) [7, 35]. This increase in spatial density of devices causes inevitably more stress on the maintenance of their operation, affecting at first their power supply, as a surging number of devices requires energy to continue sensing in order to guarantee an acceptable quality of service. Thus, the methods of powering up IoT-devices need to be reconsidered. Traditionally, devices are powered by mains or batteries. However, both methods are bound to obsolescence for practical reasons and environmental concerns. Regarding mains, the position of many devices does not allow such a way of energizing, e.g., under bridges, on continuously operating machinery in factories. Further, the cable-harness often adds a high extra cost in terms of operation. For example, main-powered sensors in the interior of airplanes add a considerable amount of weight, leading to increased fuel costs per flight. Battery operated systems are not only bulky, but also expensive to maintain since they need replacement and redeployment at a frequency that depends on the type of sensor and the needs of application. Additionally, batteries are non-ecological as they produce large carbon footprints, especially during their disposal. Because of the above, researchers are turning to systems of wireless and batteryless devices, which can be powered by Energy Harvesting (EH) instead of the aforementioned methods.

EH has been used decades ago for dynamos and solar panels, but it is becoming increasingly relevant on the last 5 years due to the rise of IoT in all sectors [30]. Several techniques of energy scavenging have been investigated, involving intervention (e.g., spinning, shaking) or ambient sources of energy (e.g., light, heat) [16, 29]. Further, hybrid methods of EH employing combinations of independent and correlated energy sources have been researched. Dedicated harvesting platforms have been constructed to acquire the energy of such sources [6], and dedicated testbeds are designed to accurately record and faithfully represent the traces (voltage and current) of sources of ambient energy across spatially distributed batteryless EH-devices in order for the scientists to develop and evaluate batteryless applications and services in such intermittent energy conditions [8]. Further, models are designed to account for the joint distribution of the energy that is obtained [1], and specific MAC protocols for EH wireless networks have been created [33]. For example, Amanor-Boadu *et al.* introduce a charging system for Li-ion batteries that uses a pulse charger, switching between an ac-adapter and a micro energy harvester of high output current [2]. Nguyen *et al.* utilize RF-harvesters and solar cells to power up rechargeable batteries and provide longer flight endurance to unmanned aerial vehicles [25]. This thesis focuses on networks of batteryless, event-driven, EH devices. The devices are on sleep-mode or powered-off until triggered by a harvesting event, which may be the result of intervention or ambient forces. For example, Yi *et al.* propose a rotation-driven piezoelectric energy harvester which scavenges kinetic energy from the rotation of tires in order to monitor tire-pressure [38]. Kouvelas *et al.* introduce wireless and batteryless switches for the interiors of airplanes, which turn the mechanical energy of pressing the button into electrical to transmit information to flight attendants [15].

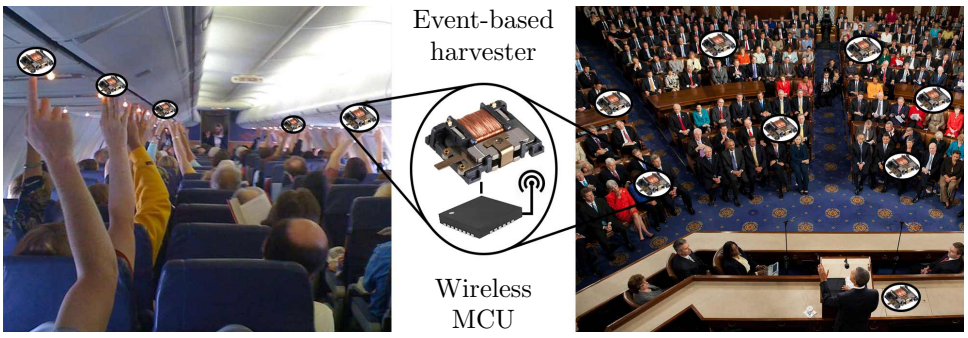

Figure 1.1. Use-cases of event driven EH sensor nodes: flight attendant call buttons (left) and voting system (right)

Future use-cases of event-driven EH nodes are seen in Figure. 1.1, where for example pressing attendant call buttons by multiple people almost concurrently, is a challenging usage scenario if not the worst-case. Or where

groups of people need to vote on-demand using EH-nodes. The high traffic load generated instantly has to be handled without packet collisions. However, current event-driven EH systems like the above –although envisioned to enable pervasive applications with high spatial density of devices– cannot guarantee the high levels of throughput required by such use-cases, as packet collisions increase humongously with the traffic load. This happens because event-driven EH systems do not allow medium sensing and message receiving due to shortage of harvested energy. Since the harvesting event does not last more than a moment, only small amounts of energy can be scavenged by such systems, e.g., clicking the button in [15] harvests at most 200μJ. Additionally, the amount of scavenged energy needs to be utilized immediately to avoid dissipation. This leads to Aloha-like systems of devices, consuming their energy budget strictly to transmit, without being aware of the channel-occupancy, and thus bounding their normalized throughput up to 0.18 because of packet collisions.

1.1 Research question

The above stated problem necessitates the need of a MAC layer protocol which bridges the gap between effective medium utilization and zero-energy needs for sensing in wireless, batteryless systems of event-driven EH-devices. This problem formalized into a single research question results in the following:

How can effective medium utilization be achieved for event driven energy harvesting wireless sensor nodes without an increase in energy budget?

1.2 Challenges

Due to the ephemeral nature of the energy source, there are several challenging issues which are both unique to the applications and remain vastly unexplored:

(a) Short active period, i.e., the energy is dissipated out of the capacitor in a few hundred ms ($\approx$300 ms) even if unused.

(b) Harvested energy is insufficient except for transmitting bare minimum information once or twice, not allowing any feedback mechanisms like acknowledgments and/or RTS/CTS.

(c) The devices need to operate asynchronously. Creating a network or coordinating actions between nodes is not possible.

Chapter 2

Related work

Event-driven harvesting devices and applications: Yi *et al.*, propose piezoelectric energy harvester, which scavenges kinetic energy to monitor tire-pressure [38]. Recently there is an interest in batteryless and wireless switches for the interiors of airplanes, which harvest the mechanical energy of pressing the button to transmit information to flight attendants [15]. Indeed Airbus is experimenting with WSNs for non-critical applications for sometime already. However, event-driven EH devices – although envisioned to enable pervasive applications with a high spatial density of devices – cannot guarantee the high levels of throughput as packet collisions increase with the traffic.

RF Harvesting: We first mention here some existing works that are close enough and employ RF harvesting. Many works in the literature have dedicated harvesting or opportunistically harvest in order to cover (partly) their energy needs [19]. Many works that employ RF harvesting use the same RF front-end for both energy scavenging and communication. Thus the focus is on finding the optimal ratio of time between harvesting and transmission so as to maximize throughput and achieve energy efficiency [17, 31, 24, 11, 3, 10].

Typically connected with RF harvesting systems are intermittent computing systems [20], however, in our applications, there is only one atomic operation of transmitting the event data. Furthermore, unlike intermittent computing systems, the nodes do not have the energy to be operational if there is no event.

Wake-up Radios: Our solution shares similarities with Wake-up Radio devices (WuR). WuR based devices get access to the channel explicitly when there is a wake-up command on the wake-up radio front-end. In literature, we find many WuR receivers operating with minimum active components

Table 2.1
Comparison of RF-DiPaQ to MAC protocols based on RF harvesting and WuR receivers
(R: Real-case, S: Simulation, N: Numerical)

	Throughput per Node	Normalized Throughput	Low Power Consumption	Less Overhead	Distributed	No Semantic Addressing	Evaluation Type
Kwan [17]	6.4bps	-	✓ ✓ ✓	✓ ✓	✓	✓	**R, S**
Naderi [24]	320bps	-	✓	✓	✓ ✓	✓ ✓	**R, S**
Hoang [11]	-	0.45	✓	✓	✓ ✓	✓ ✓	**N**
Bae [3]	-	0.16	✓	✓	✓ ✓	✓ ✓	**N**
Ha [10]	40bps	-	✓	✓	✓	✓	**S**
Le [18]	64-68bps	-	✓ ✓	✓	✓ ✓	✓	**S**
Karvonen [13]	64-68bps	-	✓ ✓	✓	✓ ✓	✓	**S**
Oller [27]	144bps	-	✓ ✓	✓	✓ ✓	✓	**S**

having up to -56 dBm of sensitivity while consuming around 1 μW on the ISM frequency bands [21, 5, 34, 18, 27]. Mangal *et al.*, fabricated a custom WuR receiver that consumes only 0.42 nW at 434 MHz with a sensitivity of -79.1 dBm [22]. Moody *et al.*, optimized for sensitivity resulting in a -106 dBm sensitive WuR operating at 428.3 MHz and consuming only 33 nW [23]. While the above WuRs need low amounts of power to operate, Zgaren *et al.*, designed an entirely passive WuR achieving a -43 dBm sensitivity at 920 MHz [39]. The concept of waking up wireless nodes from a deep sleep state to transmit – while trading-off latency in transmission with energy efficiency and thus increased lifetime – is not new [32]. Similarly, the current MAC protocols based on WuR solve the energy-intensive issue of idle-listening in wireless sensing systems, by having WuR receivers activating the primary radios of devices only when required [9, 34, 13, 18, 27]. However, almost all of the solutions use a low power active radio.

To the best of our knowledge, no MAC protocol solves the challenges of event-driven EH systems. Which leaves a void in the realm of MAC protocols for a class of extremely energy-constrained, energy-harvested IoT applications.

Chapter 3

System and principle

While Aloha-based MAC would be an obvious choice, Aloha does not scale with the offered load on the channel. On the other hand, the nodes do not have the luxury of actively switching on the radio to sense the channel for utilizing any listen-before-talk mechanisms. Further, the harvested energy is highly insufficient to keep the node operational for long duration, even in sleep mode, with one event trigger. We present Radio Frequency-Distance Packet Queuing (RF-DiPaQ), an ultra low-power MAC protocol for networks of event-driven energy-harvesting devices. The key novelty in its design is the notion of *RF information harvesting*. Through special-purpose harvesting support, we make use of the energy harvested from ongoing transmissions as information to (1) assess the occupancy of the channel, and (2) coordinate multiple concurrent transmitters.

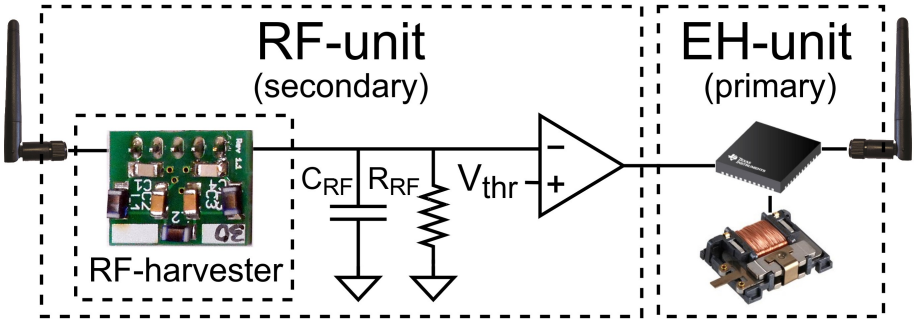

Figure 3.1. High level hardware overview of our event-driven energy harvesting node equipped with RF information harvesting unit

3.1 Hardware overview

Figure. 3.1 presents the hardware overview of a RF-DiPaQ sensor, in which two coordinating units are considered:

1. *Event-driven EH unit*: It is the primary harvester, which scavenges energy, stores it temporarily, and uses it only to transmit. The EH design involves harvesters able to transform any type of energy produced by an event into electrical energy, which is stored in supercapacitors briefly and used to power a transmitter reporting the event or sensed data. We consider the class of EH where the energy is just sufficient to transmit a few packets only, without any energy left for other functionality, including distributed coordination.

2. *RF-unit:* It is the secondary RF harvester, which involves an RF-harvesting antenna, a matching circuit, and a reference capacitor circuit that effectively represents a hardware implementation of RF information harvesting (see C_{RF}, R_{RF} in Figure. 3.1). The harvesting antenna scavenges energy whenever other devices in the vicinity transmit a packet using a Wake-up Radio (WuR) like receiver circuit charging the reference capacitor, C_{RF}, that otherwise gets discharged by resistor R_{RF}. When the reference capacitor C_{RF} discharges below a certain threshold, an idle channel is assessed (see V_{thr} in Figure. 3.1) triggering the transmission of the packet by the host device.

Assessing the occupancy of a channel in order to transmit was first introduced by Kleinrock and Tobagi, who established the Channel-Sensing Multiple Access (CSMA) protocols, in which each device senses the medium for ongoing transmissions before it transmits [14]. Nevertheless, CS is energy consuming due to active radio which is undesirable for the battery-less IoT-devices. The CSMA variants are of two types: persistent (p) and non-persistent (np). In p-CSMA each device pending to transmit senses the medium continuously until it becomes idle, and then transmits with probability p; if $p = 1$, then the device transmits unconditionally, i.e., 1-CSMA. In the np case, a device backs off for a random duration when the medium is sensed busy and transmits when the medium is sensed free. Inherent assumption in these protocols is that devices are in the sensing range of each other. Similar to the 1-CSMA, devices employing RF-DiPaQ refrain from transmission until the medium is idle, and then transmit unconditionally. However, contrary to 1-CSMA where the medium is continuously sensed by a device pending to transmit, RF-DiPaQ performs indirect sensing by observing the voltage-level of the reference capacitor that is charged by the devices occupying the medium. Therefore, RF-DiPaQ networks enjoy the increased throughput offered by CSMA protocols, without paying the price of energy consumption due to continuous sensing. Furthermore, since the level

up to which the reference capacitor is charged depends on multiple reasons –the distance of each RF-DiPaQ device from the transmitting source, the timing of packet arrivals, and the transmitting conditions– each device gets charged up to a different level. This leads to different times of discharging down to threshold-voltage, allowing only one device to transmit at a time, thus avoiding collisions which would be inevitable in 1-CSMA. Table 3.1 sums up the comparison of our RF-DiPaQ MAC to classical Aloha, 1-CSMA, and np-CSMA, highlighting that RF-DiPaQ is the preferable protocol to increase throughput consuming ultra low energy under the constraints given by EH networks and RF harvesting.

Table 3.1
Comparison of RF-DiPaQ to main channel contention protocols

	RF-DiPaQ	Aloha	1-CSMA	np-CSMA
High Throughput	✓ ✓	✗	✓	✓ ✓ ✓
Low Consumption	✓ ✓ ✓	✓ ✓ ✓	✗	✓
Large Sensing Distance	✓	-	✓ ✓	✓ ✓
Low Complexity	✓	✓ ✓	✗	✗

3.2 RF Information Harvesting

We introduce the term "RF information harvesting" because, to the best of our knowledge, this is the first time that the scavenged energy from a source –non-dedicated RF transmissions in our case– is utilized to infer the condition of the medium instead of performing radio operations.

In RF information harvesting, the received carrier wave is rectified by a RF harvesting circuit and used to charge a reference capacitor (C_{RF}), which is continuously being discharged by a resistor (R_{RF}). This results in the voltage across C_{RF}, denoted by V_{RF}, to vary depending on the channel activity. V_{RF} is compared to a close-to-zero voltage-threshold (V_{thr}). When a carrier wave is being received, V_{RF} exceeds V_{thr}, indicating that the channel is being utilized by a neighboring node. On the other hand, if no carrier wave is being received, V_{RF} drops below V_{thr}, indicating a clear channel. The RF information harvesting can be done passively even while the MCU is not powered. This enables detecting the channel activity at the expense of negligible energy ($\sim$nJ). The schematic diagram of the hardware needed for the RF-DiPaQ protocol is depicted in Figure. 3.1. Note in Figure. 3.1 that RF-DiPaQ provides a dedicated system of sensing that utilizes RF information harvesting strictly for channel sensing, without interfering with the EH-unit of a device or requiring a portion of its harvested energy which is used for transmission. However, the antenna for the RF information harvesting can also be shared with the wireless MCU to save on area, but due to the need for a RF-switch this would decrease the sensitivity of the

system.

3.3 Radio Frequency-Distance Packet Queuing

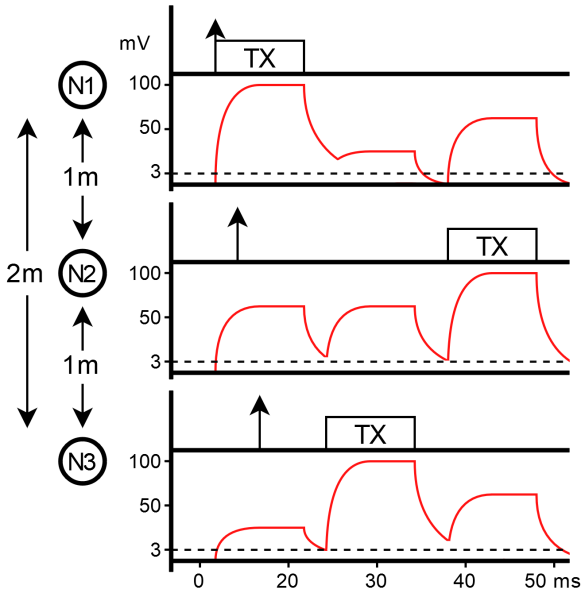

Figure 3.2. RF activity and charge in C_{rf} over time for three transmitting nodes, following the RF-DiPaQ protocol

RF-DiPaQ device relies on the outcome of RF information harvesting for transmitting packets. In Figure. 3.2, we illustrate the working of media access mechanism of RF-DiPaQ in a network involving three RF-DiPaQ nodes. The figure shows RF activity and the temporal variation of V_{RF} for the three nodes, denoted as *N1*, *N2*, and *N3*. MAC frame arrivals are indicated by upward pointing arrows and the *TX* block indicates packet transmissions. Let the nodes be placed linearly with a distance of 1 m between adjacent nodes. The first packet to arrive from N1 is transmitted immediately as the corresponding V_{RF} is below the $V_{\mathrm{thr}} = 3\,\mathrm{mV}$. While this transmission is ongoing, MAC frames arrive at N2 and N3. Note that V_{RF} depends on the distance of the node from N1; smaller distance implies higher voltage and vice-versa. Once N1's transmission is complete, V_{RF} at each node starts to drop continuously. Due to its lower value, V_{RF} of N3 drops below V_{thr} first. Since a pending node may only transmit when $V_{\mathrm{RF}} \leq V_{\mathrm{thr}}$, N3 will begin its transmission before N2. This causes the V_{RF} across the other two nodes to rise, further postponing N2's transmission. Once N3 completes its transmission, V_{RF} of N2 drops below V_{thr}, causing N2's transmission to begin. Theoretically, two or more equidistant nodes could have same values for V_{RF}, in which case all of them will start to transmit simultaneously, res-

ulting in collisions. However, in practice, due to multi-path fading and the presence of (moving) obstacles, two equidistant nodes are rarely charged to the same V_{RF}. This ensures collision avoidance.

Chapter 4

Implementation and validation

To evaluate the performance of RF-DiPaQ, nine nodes with RF information harvesting hardware were built (see Figure. 4.1) and programmed to follow the RF-DiPaQ protocol. Their performance and the charges in their reference capacitors C_{RF} were measured in sets of three and nine nodes. We adapt a specific RF-unit circuit shown in Figure. 4.2, based on the design proposed by Nintanavongsa *et al.* [26]. This design was chosen for its simplicity and ability to be build with off-the-shelf components.

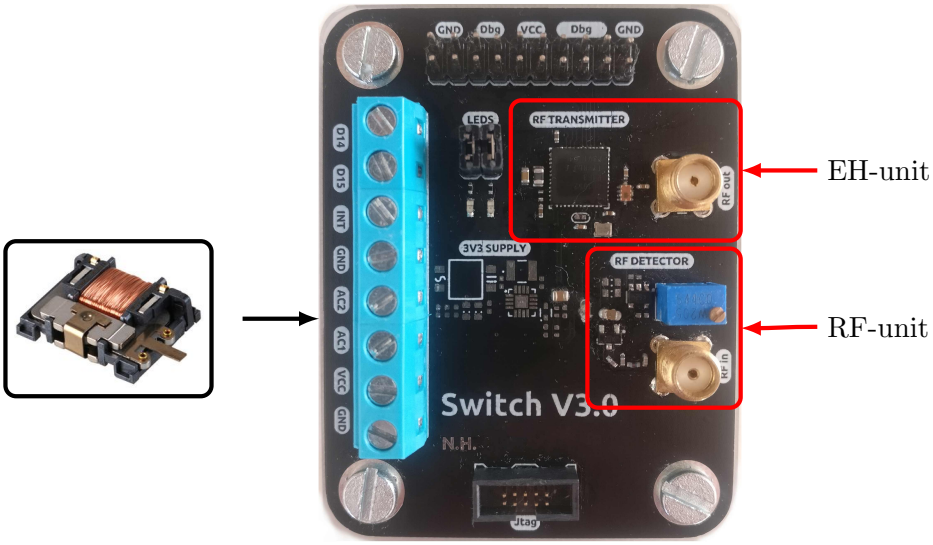

Figure 4.1. Picture of the Switch V3.0, a prototype of wireless sensor node with a RF information harvesting RF-unit able to run the RF-DiPaQ MAC protocol

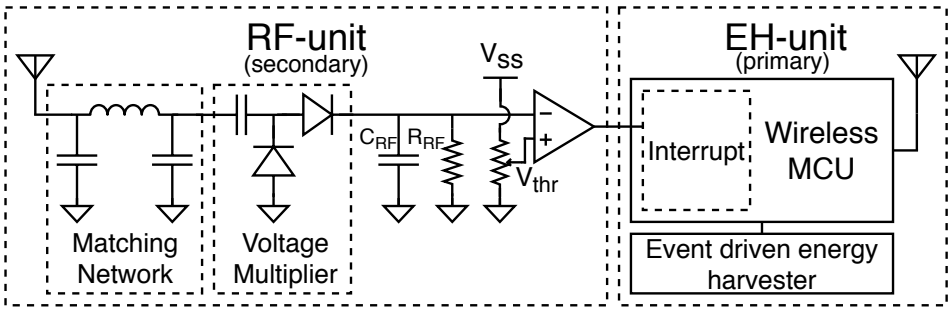

Figure 4.2. Hardware overview of our implementation of an event-driven energy harvesting sensor node equipped with RF information harvesting hardware based on off-the-shelf components

The antenna is connected to a pi-matching network which tunes the RF-unit to the specific carrier wave frequency. Using a single-stage voltage multiplier the RF signal is rectified, doubled, and used to charge capacitor C_{RF}. Resistor R_{rf} discharges C_{RF} when no carrier wave is received. An inverting comparator compares the voltage in C_{RF} to the threshold voltage V_{thr}. The level of V_{thr} can be tuned by adjusting a potentiometer. The comparator outputs a digital-high when the voltage in C_{RF} is lower than V_{thr} and a digital-low when higher. The digital output of the comparator is connected to one of the interrupt pins of the wireless MCU. The CC1352R [12] is chosen as wireless MCU, which is programmed to transmit immediately when the comparator output is high or sleep until a rising flank, and then transmit.

4.1 3-node validation

To validate the RF-DiPaQ protocol, the scenario shown in Figure. 3.2 was tested with three Switch V3.0 nodes. In this test scenario, three packets arrive within one packet time which would cause collisions in a 1-CSMA MAC-system. Figure. 4.3 shows the voltage in the capacitor of node-2, $C_{RF}^{(2)}$, (light blue), the voltage in the capacitor of node-3, $C_{RF}^{(3)}$, (dark blue) and the digital output of the comparators of node-2 (yellow) and node-3 (pink) over time. Node-1 was programmed to arrive immediately and nodes 2 and 3 to arrive during node-1's transmission.

Figure. 4.3 shows the initial transmission by node-1 (indicated by the "1") resulting in the rising of the voltage-levels in both reference capacitors C_{RF}. As node-2 is closer to node-1 compared to node-3, $C_{RF}^{(2)}$ is charged higher. Thus, when node-1 finishes transmitting and the voltages in the reference capacitors C_{RF} start to drop, the voltage in $C_{RF}^{(3)}$ will reach the threshold-voltage (dashed line) before the voltage in $C_{RF}^{(2)}$. The moment the voltage in

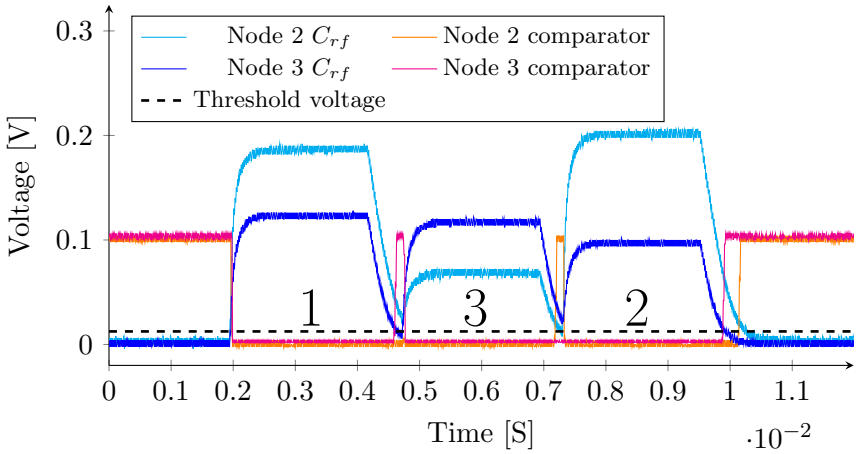

Figure 4.3. Measured voltages in two C_{rf}s and their digital comparator outputs (scaled down) over time, while three messages are transmitted by three different nodes, showing distance-based prioritization

$C_{RF}^{(3)}$ goes below the threshold-voltage the comparator of node-3 outputs a digital-high, allowing node-3's MCU to transmit. The transmission by node-3, indicated with the "3", causes the voltages in all reference capacitors C_{RF} to rise again. This results in the voltage in $C_{RF}^{(2)}$ to not down-pass the threshold voltage, keeping node-2's comparator output at digital-low. During the transmission of node-3, since it is closer to itself than node-2, $C_{RF}^{(3)}$ is charged higher than $C_{RF}^{(2)}$. Thus, when node-3 finishes transmitting, and assuming that node-1 has no packet pending, the voltage in $C_{RF}^{(2)}$ down-passes the threshold voltage first, causing node-2's comparator to output a digital-high, allowing node-2's MCU to transmit. The transmission of node-2 again causes all the charges in the reference capacitors C_{RF} to rise, this time preventing the charge in $C_{RF}^{(3)}$ to reach the threshold voltage, and thereby not triggering its comparator. If node-3 had to transmit again, it would wait until after the transmission of node-2. During node-2's transmission, indicated with the "2", $C_{RF}^{(2)}$ is charged higher than $C_{RF}^{(3)}$, since node-2 is closer to itself than node-3. As there are no more packets to be transmitted, once node-2 finishes transmitting the voltages in all reference capacitors C_{RF} drop to zero causing all comparators to output digital-high, indicating an idle channel. The previously described behavior as shown in Figure. 4.3 is the same as shown in Figure. 3.2, confirming the way of operation of the RF-DiPaQ protocol as described in Section 3.3.

4.2 Network validation

At high values of offered load g, using 1-CSMA, there is an increasing probability of transmissions ending with multiple pending packets which will result in collisions. This is however not the case when using RF-DiPaQ, as described in Section 3.3, and results in RF-DiPaQ outperforming 1-CSMA.

At higher values of g the performance of RF-DiPaQ is limited by the average C_{RF} discharge time of the lowest charged pending node, as this equals the not-utilised time between two successive transmissions. Furthermore, it is also limited by the probability of two pending nodes being charged to the same voltage, which would result in a collision. This probability depends on the number of pending nodes, environmental, and hardware factors, i.e., pathloss exponent, transmission power, RF-harvesting efficiency and load impedance. Utilizing large numbers of nodes increases the probability of two pending nodes being charged to the same voltage. Therefor, the throughput of a RF-DiPaQ network is expected to approach zero for networks with a large number of nodes at high values of g.

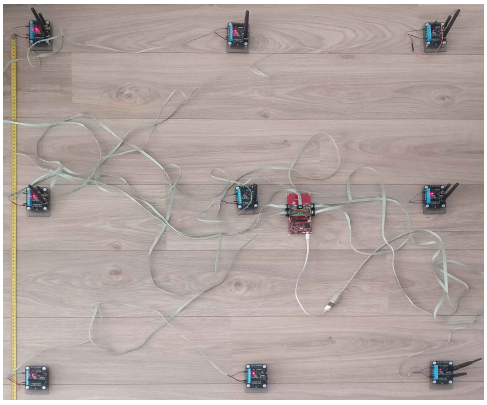

Figure 4.4. Picture of nine RF-DiPaQ nodes in a 1 m by 1 m area, connected with wires to a gateway emulating multiple harvester events per second

To validate the aforementioned expectations regarding the performance of RF-DiPaQ, a network of nine RF-DiPaQ nodes was built and tested. Nine Switch V3.0, as shown in Figure. 4.1, were placed within an one square-meter area with the gateway close to the middle, as shown in Figure. 4.4. All nodes are connected to the gateway using wires, enabling the gateway to emulate multiple harvester events per second at all nine nodes at the same time. This area was chosen because the RF-unit circuit of the Switch V3.0 is built by off-the-shelf components and is only sensitive down to -40 dBm. Prospective applications of such device distributions are found in wireless body area networks. The research interest on EH is growing in such networks to power up wearable sensors placed on different positions of the body to

measure temperature, heartbeat, acceleration etc. in order to improve health and lifestyle [17, 36]. RF-DiPaQ devices would be ideal candidates for EH body area networks. In our experiment, all nine nodes are powered over cables connected to the gateway, and programmed to simulate X arrivals at a $g/9$ Poisson arrival rate using their on-board timers. The gateway is programmed to count the number of successfully received packages and reports the count divided by $(X \cdot 9)$ back to a PC as the success rate for this particular offered load g. The success rate at a particular g can be multiplied with g to get the network throughput.

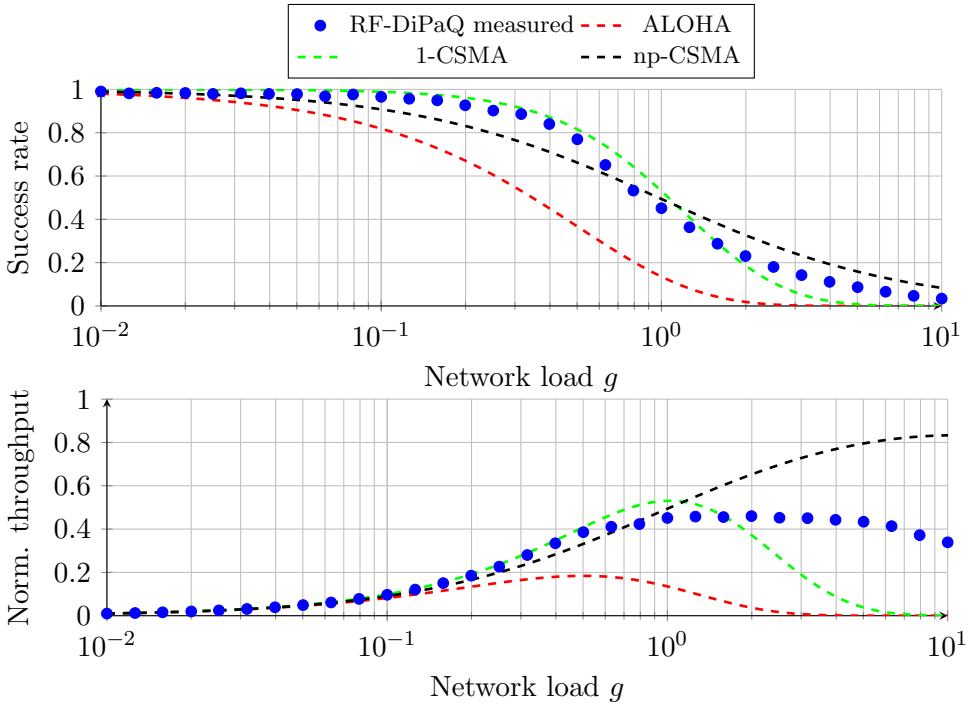

Figure 4.5. Measured success rate (top) and norm. throughput (bottom) over network load compared to other protocols

As observed in the success rate in Figure. 5.5, the performance of the RF-DiPaQ network is similar to 1-CSMA up to $g = 10^0$, after which it outperforms 1-CSMA as clearly seen in the throughput in Figure. 5.5, confirming the expectations of RF-DiPaQ superiority in higher traffic. The throughput of the nine RF-DiPaQ node network, as shown in Figure. 5.5, remains constant after $g = 10^0$, with a small decrease close to $g = 9$. This decrease happens because with nine nodes no arrival rate of more than nine is possible, as this would result in arrivals while nodes are still transmitting. As the arrival rate is described by the packet time not including the discharge time between transmissions, this point is reached just before $g = 9$. The throughput remains constant after $g = 10^0$ due to the network exist-

ing out of a relatively small number of nodes. This reduces the number of different voltages the reference capacitors C_{RF} will be charged to, resulting in a limited number of collision combinations. The throughput is limited by the average discharge time between two successive transmissions. As this unutilised time does not depend on offered load g, the throughput remains constant. When the area and number of nodes increases, the range of voltage-values the reference capacitors C_{RF} are charged to also increases, resulting in more collision combinations. This will result in the throughput approaching zero at high levels of g for large networks.

Chapter 5

Model

In order to evaluate the limiting performance of RF-DiPaQ in a network involving multiple EH devices, a model of the MAC protocol is developed. The state diagram of the model is shown in Figure. 5.1. We calculate the average time and probability of success for each state. Together with the steady state probabilities, the success rate and throughput for a given offered load g can be numerically found, by extending the 1-CSMA model by Cheung [4].

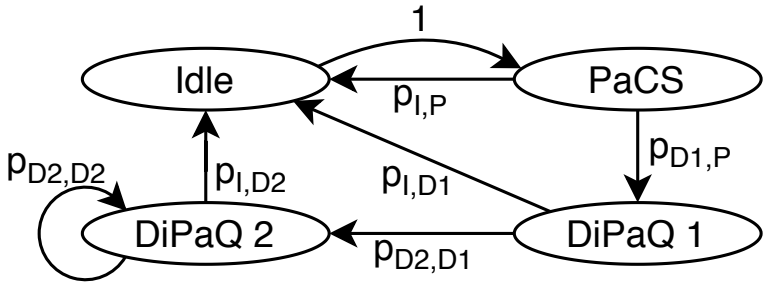

Figure 5.1. Model state diagram

5.1 Model overview

Figure. 5.1 shows the model state diagram. The model has four states: Idle, Passive Carrier-Sense Multiple-Access (PaCS), and two RF-DiPaQ states. In the Idle state there are no packets in the system and the charges in the C_{RF}s of all N nodes are below V_{thr}. Since RF-DiPaQ depends on the charges in the C_{RF}s remaining from the previous transmission, the Packet Queuing Effect is not active in the first state after an Idle period. Therefor the first state after an Idle state is the non-RF-DiPaQ PaCS state. After PaCS, the system can proceed to the RF-DiPaQ states. As the success probability

of the RF-DiPaQ protocol depends on the number of pending packets the previous state ended with, the RF-DiPaQ state is split in two: DiPaQ 1 and DiPaQ 2, where DiPaQ 1 transitions from the PaCS state and DiPaQ 2 from either DiPaQ 1 or 2.

Table 5.1 summarizes the formal state transition conditions with $\sum_P$ being the total number of pending packets, C the set of charge levels in all reference capacitors C_{RF}, and C_p a subset of C holding the set of charges in the reference capacitors C_{RF} of all nodes with a pending packet. Idle transitions into PaCS, the moment the first packet arrives. All non-idle states transition back to the Idle state when ending with zero pending packets, the moment the highest charged node discharges down to V_{thr}. The moment the lowest charged pending node discharges down to V_{thr} and commits to transmit, all non-idle states transition into the next non-idle state. Figure. 5.2 depicts how the arrivals, commitments, and discharge times line up with the state transitions.

Table 5.1
State transition conditions

From	To	Condition
Idle	PaCS	$\sum_P = 1 \wedge \forall c \in C : c < V_{thr}$
PaCS	Idle	$\sum_P = 0 \wedge \forall c \in C : c < V_{thr}$
PaCS	DiPaQ 1	$\sum_P > 0 \wedge min(C_p) = V_{thr}$
DiPaQ 1	Idle	$\sum_P = 0 \wedge \forall c \in C : c < V_{thr}$
DiPaQ 1	DiPaQ 2	$\sum_P > 0 \wedge min(C_p) = V_{thr}$
DiPaQ 2	Idle	$\sum_P = 0 \wedge \forall c \in C : c < V_{thr}$
DiPaQ 2	DiPaQ 2	$\sum_P > 0 \wedge min(C_p) = V_{thr}$

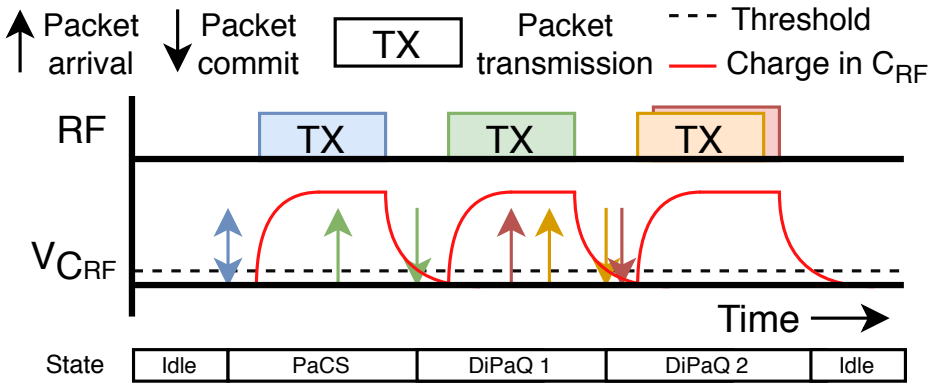

Figure 5.2. Simplified example of system states over time while packets arrive, and their effect on $V_{C_{RF}}$

$$T_h = \frac{\sum_{i=0}^{3} \pi^i \cdot T \cdot P(\text{success in } S_i)}{\sum_{i=0}^{3} \pi^i \cdot \underline{T^i}} \tag{5.1a}$$

$$S = T_h / g \tag{5.1b}$$

To model the performance of the RF-DiPaQ protocol Equation. 5.1a and Equation. 5.1b can be used to calculate the system throughput T_h and success rate S, based on steady state probabilities π^i, packet transmission time T, the state success probabilities, and the expected state times $\underline{T^i}$, with $i = 0, 1, 2, 3$ representing the states: Idle (I), PaCS (P), DiPaQ 1 ($D1$), and DiPaQ 2 ($D2$) respectively.

5.2 State time and probability of successful transmissions

First we'll show how to find the state success probabilities and the expected state times based on a given load g, the number of all old and new packets arriving per packet time T, according to a Poisson process.

5.2.1 Idle

The average time of the Idle state $\underline{T^I}$, is the average time of no arrivals, and can be calculated as shown in Equation. 5.2 due to the arrivals emerging from a Poisson process. In the Idle state no packets are transmitted so the probability of a successful transmission equals zero, see Equation. 5.3.

$$\underline{T^I} = \frac{1}{g} \tag{5.2}$$

$$P(\text{success in Idle}) = 0 \tag{5.3}$$

5.2.2 PaCS

Figure. 5.3 zooms in to the four time segments which together form the expected PaCS state time $\underline{T^P}$, see Equation. 5.4. As the PaCS state always follows an Idle period the charges in all C_{RF}s start below the threshold, causing the first arrival to immediately commit to transmit starting the PaCS state. As it takes time for a radio to start-up before it is able to transmit, there is a vulnerable time period between a node committing and transmitting. This time normalised to T, τ results in there being a probability of other nodes arriving and committing before the first packet is transmitted. Only once the first packet being transmitted do the charges in the C_{RF}s

rise above V_{thr}, preventing other nodes from committing to transmit. The first time segment of the PaCS state, y^P, represents the difference in time between the first and last arrival within the vulnerable period of τ time after the first arrival. After y^P it takes τ plus T time for the last transmission to finish. The PaCS state ends either in case 0 (i.e., zero packets pending), resulting in the Idle state or in case 1 (i.e., at least 1 pending), resulting in the DiPaQ 1 state. Case 0 and 1 have different expected discharge time $E[T_{rc}]$.

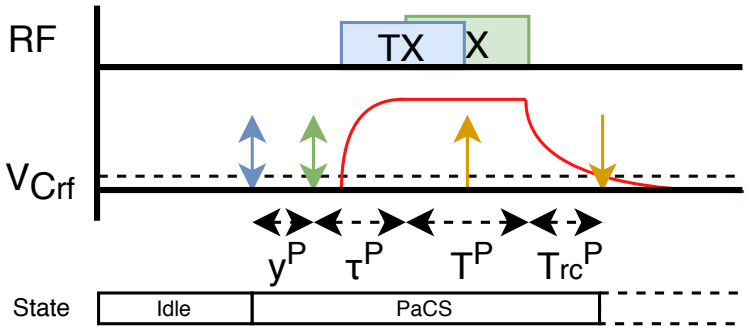

Figure 5.3. Close up from Figure. 5.2 showing time segments of the PaCS state

$$\underline{T^P} = E[y^P] + \tau + T + E[T_{rc}^P] \tag{5.4}$$

As τ and T are constants determined by the chosen radio and packet structure, only $E[y^P]$ and $E[T_{rc}^P]$ need to be found. Equation. 5.5 shows the cumulative distribution function (CDF) of y^P which equals the probability of no arrivals in time $\tau - t$. Note that this CDF only holds for the range $t \in (0, \tau]$ as y^P is a hybrid random variable being discontinuous at $t = 0$. Equation. 5.7 shows the probability of $y = 0$ which equals the probability of no arrivals in time τ. The probability density function (PDF) over the full range of $t \in [0, \tau]$ is shown in Equation. 5.8 with $\delta(t)$ being the delta function. The expected value of y^P is calculated in Equation. 5.9.

$$F_{y^P}(t) = e^{-g(\tau - t)} \text{ , for } t \in (0, \tau] \tag{5.5}$$

$$\begin{aligned} f_{y^P}(t) &= \frac{de^{-g(\tau-t)}}{dt} \\ &= ge^{-g(\tau-t)} \text{ , for } t \in (0, \tau] \end{aligned} \tag{5.6}$$

$$f_{y^P}(0) = e^{-g\tau} \tag{5.7}$$

$$f_{y^P}(t) = e^{-g\tau}\delta(t) + ge^{-g(\tau-t)} \text{ , for } t \in [0, \tau] \tag{5.8}$$

$$
\begin{aligned}
E[y^P] &= \int_0^\tau t f_{y^P}(t) dt \\
&= \tau - \frac{1 - e^{-g\tau}}{g}
\end{aligned}
\tag{5.9}
$$

$E[T_{rc}^P]$ depends on the discharge times of the C_{RF}s. For this model it is assumed that the voltage to which the capacitors are charged V can be expressed in terms of input power P_{in} as shown in Equation. 5.10 as measured by Del Prete *et al.* [5], with a, b being hardware constants.

$$
V = 10^{a \cdot P_{in} + b} \tag{5.10}
$$

Assuming the pathloss model, P_{in} can be expressed in terms of distance to the transmitter d, resulting in Equation. 5.11. Which is simplified to Equation. 5.12, where V is expressed in terms of k and l which can also be found by measurement.

$$
\begin{aligned}
&V = 10^{m_1} \\
&\quad \text{for } m_1 = a \cdot (P_{tx} - P_{l0} + 10 \cdot P_{le} \cdot log_{10}(d/d_0)) + b
\end{aligned}
\tag{5.11}
$$

$$
V = d^k \cdot l \tag{5.12a}
$$

$$
k = -a \cdot 10 \cdot P_{le} \tag{5.12b}
$$

$$
\begin{aligned}
&l = 10^{m_2} \\
&\quad \text{for } m_2 = a \cdot (P_{tx} - P_{l0} + 10 \cdot P_{le} \cdot log_{10}(d_0)) + b
\end{aligned}
\tag{5.12c}
$$

Assuming the discharge of C_{RF} follows a perfect RC discharge curve, it's charge over time can be described by Equation. 5.13, with the $RC = C_{rf} \cdot R_{rf}$ as shown in Figure. 4.2. The discharge curve can be rewritten to find T_{rc}, the time it takes for the voltage in a node's C_{RF} to discharge down to the threshold voltage V_{thr}, starting at voltage V, after a transmission ends. By substituting V with Equation. 5.12, T_{rc} can be expressed in terms of distance, resulting in Equation. 5.14a. T_{rc} can be seen as a transformation on D with function $g(d)$ shown in Equation. 5.14b, where D is a random variable representing the inner node distances. Assuming the distribution of D known, the PDF and CDF of T_{rc} can be calculated as shown in Equation. 5.15 and Equation. 5.16.

$$
v(t) = v_{start} e^{-t/RC} \tag{5.13}
$$

$$T_{rc} = \frac{RC}{T} \cdot ln(\frac{D^k \cdot l}{V_{thr}}) \tag{5.14a}$$

$$g(d) = \frac{RC}{T} \cdot ln(\frac{d^k \cdot l}{V_{thr}}) \tag{5.14b}$$

$$\begin{aligned} f_{Trc}(t) =& - f_D(g^{-1}(t)) \frac{\delta}{\delta t} g^{-1}(t) \\ =& - f_D((e^{t \cdot T/RC} \cdot \frac{V_{thr}}{l})^{1/k}) \cdot \\ & \cdot ((e^{t \cdot T/RC} \cdot \frac{V_{thr}}{h})^{1/k}) \cdot \frac{T}{k \cdot RC} \end{aligned} \tag{5.15}$$

$$\begin{aligned} F_{Trc}(t) =& 1 - F_D(g^{-1}(t)) \\ =& 1 - F_D((e^{t \cdot T/RC} \cdot \frac{V_{thr}}{l})^{1/k}) \end{aligned} \tag{5.16}$$

With distribution of T_{rc} known, the expected value of the discharge time for both case 0 and 1 is calculated. In case 0 the next state will be Idle. This means $T^P_{rc,0}$ equals the discharge time of the highest charged C_{RF} of all N nodes. The expected value of the maximum of multiple samples of the same distribution is found using order statistics in Equation. 5.17 and Equation. 5.18, with $f_{T_{rc}}(x)$ being the PDF and $F_{T_{rc}}(x)$ the CDF of T_{rc}.

$$P(T^P_{rc,0} = x) = N f_{T_{rc}}(x) \cdot F_{T_{rc}}(x)^{N-1} \tag{5.17}$$

$$E[T^P_{rc,0}] = \int_0^\infty x N f_{T_{rc}}(x) \cdot F_{T_{rc}}(x)^{N-1} dx \tag{5.18}$$

In case 1 the next state will be DiPaQ 1. This results in $T^P_{rc,1}$ equaling the discharge time of the lowest charged C_{RF} of all n pending nodes. The minimum of n samples from T_{rc} is found using order statistics in Equation. 5.19 and Equation. 5.20.

$$P(T^P_{rc,1} = x|n) = n \cdot f_{T_{rc}}(x) \cdot (1 - F_{T_{rc}}(x))^{n-1} \tag{5.19}$$

$$E[T^P_{rc,1}|n] = \int_0^\infty x \cdot n \cdot f_{T_{rc}}(x) \cdot (1 - F_{T_{rc}}(x))^{n-1} dx \tag{5.20}$$

To find $E[T^P_{rc,1}]$, the probability of the PaCS state ending with n pending nodes, $P(N_{\text{PaCS}} = n)$ needs to be found. Because all arrivals during the

first τ time of the state immediately transmit, this equals the probability of n arrivals in $\underline{T^P} - \tau$ time. As $E[T^P_{rc,1}]$ is yet not known, but is part of $\underline{T^P} - \tau$, an estimate of $\underline{T^P} - \tau$, $\underline{T^P_{\text{est}}}$, is used to estimate $P(N_{\underline{T^P} - \tau} = n)$ with $P(N_{\underline{T^P_{\text{est}}}} = n)$. Because the PaCS state has a higher steady state probability at lower values of load g, $E[T^P_{rc,0}]$ is chosen as an estimate of $E[T_{rc}]$ to form $\underline{T^P_{\text{est}}}$ as case 0 is also more dominant at lower values of load g, see Equation. 5.21.

$$\underline{T^P} - \tau \approx \underline{T^P_{\text{est}}} = E[y^P] + T + E[T^P_{rc,0}] \tag{5.21}$$

Given the state is ending in a case 1 scenario and the network exists out of N nodes, there must have been at least 1 and at most N arrivals within $\underline{T^P_{\text{est}}}$. So the probability of n arrivals in $\underline{T^P_{\text{est}}}$ must be divided by the sum of probabilities of 1 to N arrivals. This can be calculated with function $A(n, t, m)$ as shown in Equation. 5.22, which calculates the probability of n arrivals in t time given at least m arrivals. $A(n, t, m)$ is calculated as shown in Equation. 5.23, where $P(x \text{ in } t)$ stands for the Poisson PDF calculating the probability of x arrivals in t time. With the probabilities of n arrivals given case 1 known, $E[T^P_{rc,1}]$ is calculated in Equation. 5.24.

$$P(N_{\underline{T^P_{\text{est}}}} = n) = A(n, \underline{T^P_{\text{est}}}, 1) \tag{5.22}$$

$$\begin{aligned} A(n, t, m) &= \frac{P(n \text{ in } t)}{\sum_{i=m}^{N} P(i \text{ in } t)} \\ &= \frac{\frac{(gt))^n}{n!} e^{-gt}}{\sum_{i=m}^{N} \frac{(gt))^i}{i!} e^{-gt}} \end{aligned} \tag{5.23}$$

$$E[T^P_{rc,1}] = \sum_{n=1}^{N} A(n, \underline{T^P_{\text{est}}}, 1) \cdot E[T^P_{rc,1} | pn] \tag{5.24}$$

The probabilities of case 0 (P^P_0) and case 1 (P^P_1) occurring can be found in Equation. 5.25 and Equation. 5.26, making use of function $A(n, t, m)$ found in Equation. 5.23, which calculates the probability of 0 arrivals in $\underline{T^P_{\text{est}}}$ time, given at least 0 arrivals. Equation. 5.27 shows how these probabilities are used to find the expected value of the T^P_{rc} in the PaCS state. $E[y^P]$ and $E[T^P_{rc}]$ together with τ and T can now be filled into Equation. 5.4 to find the expected state time of the PaCS state, $\underline{T^P}$.

$$P_0^P = A(0, \underline{T_{\text{est}}^P}, 0) \tag{5.25}$$

$$P_1^P = 1 - P_0^P \tag{5.26}$$

$$E[T_{rc}^P] = P_0^P \cdot E[T_{rc,0}^P] + P_1^P \cdot E[T_{rc,1}^P] \tag{5.27}$$

The PaCS state always follows the Idle state, and starts on the first arrival. All arrivals within time τ after the first arrival will collide with the first packet. Any arrivals in the remaining time of the state will postpone their transmission till the next state. This results in the probability of success in the PaCS state equaling the probability of no arrivals within time τ, which is calculated with function $A(n, t, m)$ Equation. 5.23 as shown in Equation. 5.28.

$$P(\text{success in PaCS}) = A(0, \tau, 0) \tag{5.28}$$

5.2.3 DiPaQ 1

Similar to the PaCS state as shown in Figure. 5.3, the expected DiPaQ 1 state time $\underline{T^{D1}}$ is split into 4 time segments as shown in Equation. 5.29. Time segment y^{D1} is the time between the first and the last arrival of all nodes committing to transmit this period. These are determined by discharge time distribution T_{rc}. Equation. 5.30 calculates the probability of $y = t$ given n pending nodes at time τ into state DiPaQ 1.

$$\underline{T^{D1}} = E[y^{D1}] + \tau + T + E[T_{rc}^{D1}] \tag{5.29}$$

$$\begin{aligned} P(y^{D1} = t|n) = \int_0^\infty \binom{n}{2} & f_{T_{rc}}(x) \cdot f_{T_{rc}}(x+t) \\ & \cdot ((F_{T_{rc}}(x+t) - F_{T_{rc}}(x)) + (1 - F_{T_{rc}}(x+\tau)))^{n-2} dx \\ & (\text{for } n \geq 2 \text{ and } t \in (0, \tau]) \end{aligned} \tag{5.30}$$

The number of pending nodes at time τ into the DiPaQ 1 state depends on the number of arrivals in the last $\underline{T^P} - \tau$ time of the previous PaCS state plus the arrivals in the first τ time of this DiPaQ 1 state. Together the probability of n pending nodes at time τ into the DiPaQ 1 state is calculated in Equation. 5.31, where $P(x \text{ in } t)$ stands for the Poison PDF calculating the probability of x arrivals in t time. Given the current state is DiPaQ 1 there must have been at least one arrival in $\underline{T^P} - \tau$. So the probability of n pending nodes at time τ into the DiPaQ 1 state is split into the sum of a arrivals in $\underline{T^P} - \tau$ and the remainder of the $n - a$ arrivals in τ.

$$P(N_{\underline{T^P}} = n|\text{DiPaQ 1}) = \frac{\sum_{a=1}^{n} P(a \text{ in } \underline{T^P} - \tau) \cdot P(n-a \text{ in } \tau)}{\sum_{b=1}^{N}\sum_{a=1}^{b} P(a \text{ in } \underline{T^P} - \tau) \cdot P(b-a \text{ in } \tau)} \tag{5.31}$$

Equation. 5.30 and Equation. 5.31 can be combined to find the probability of $y^{D1} = t$, as shown in Equation. 5.32a. However this only holds for $t \in (0, \tau]$ as it assumes at least two arrivals. The probability of $y^{D1} = 0$ equals the probability of only one arrival as shown in Equation. 5.32b. Combining these two equations results in the probability of $y^{D1} = t$ that holds for $t \in [0, \tau]$ as shown in Equation. 5.32c.

$$P(y^{D1} = t, t > 0) = \sum_{n=2}^{N} P(N_{\underline{T^P}} = n|\text{DiPaQ 1}) P(y^{D1} = t|n) \tag{5.32a}$$

$$P(y^{D1} = 0) = P(N_{\underline{T^P}} = 1|\text{DiPaQ 1}) \tag{5.32b}$$

$$\begin{aligned} P(y^{D1} = t) =& P(N_{\underline{T^P}} = 1|\text{DiPaQ 1})\delta(t) + \\ &+ \sum_{n=2}^{N} P(N_{\underline{T^P}} = n|\text{DiPaQ 1}) P(y^{D1} = t|n) \end{aligned} \tag{5.32c}$$

With probability $P(y^{D1} = t)$ known the expected value of y^{D1} is calculated in Equation. 5.33.

$$\begin{aligned} E[y^{D1}] &= 0 \cdot P(y^{D1} = 0) + \int_{0+}^{\tau} t \cdot P(y^{D1} = t, t > 0) dt \\ &= \sum_{n=2}^{N} P(N_{\underline{T^P}} = n|\text{DiPaQ 1}) \int_{0+}^{\tau} t \cdot P(y^{D1} = t|n) dt \end{aligned} \tag{5.33}$$

Similar to PaCS, the DiPaQ 1 state ends either in case 0, see Equation. 5.18, or case 1, see Equation. 5.22 and Equation. 5.24 but with $\underline{T_{\text{est}}^{D1}}$ instead of $\underline{T_{\text{est}}^{P}}$. Equation. 5.34 shows the estimate of $\underline{T^{D1}} - \tau$, $\underline{T_{\text{est}}^{D1}}$, representing the time of the state DiPaQ 1 in which nodes arrive and will contest in the next period, influencing the time of $E[T_{rc}^{D1}]$. As $E[T_{rc}^{D1}]$ is not yet known, the estimate of $E[T_{rc,1}^{D1}|n = 2]$ is used, see Equation. 5.20. This estimate has been chosen because at higher levels of load g when state 2 is dominant, case 1 is also dominant.

$$\underline{T_{\text{est}}^{D1}} = E[y^{D1}] + T + E[T_{rc,1}^{D1}|n = 2] \tag{5.34}$$

Similar to the PaCS sate, $E[T_{rc}^{D1}]$ in the DiPaQ 1 state is calculated as in Equation. 5.25, Equation. 5.26 and Equation. 5.27 but with probability of case 0 (P_0^{D1}) and case 1 (P_1^{D1}), and $E[T_{rc,1}^{D1}]$ based on $\underline{T_{\text{est}}^{D1}}$ instead of $\underline{T_{\text{est}}^{P}}$. With $E[y^{D1}]$, $E[T_{rc}^{D1}]$, τ, and T, the actual expected state time of the DiPaQ 1 state, $\underline{T^{D1}}$, is calculated in Equation. 5.29.

The probability of success in the state DiPaQ 1 is based on the effect described in Section 3.3. The state is successful when the difference in discharge times, modeled by T_{rc} as shown in Equation. 5.15 and Equation. 5.16, of the two lowest charged nodes with a pending packet is larger than time τ. The probability of success given n nodes waiting to transmit at τ time into the state is given in Equation. 5.35. Together with the probability of n pending nodes at time τ into the DiPaQ 1 state, calculated with Equation. 5.31, the probability of success can be calculated as shown in Equation. 5.36.

$$\begin{aligned} P(\text{success in DiPaQ 1 } |n) = &\int_0^\infty n \cdot f_{T_{rc}}(x) \\ &\cdot (1 - F_{T_{rc}}(x+\tau))^{n-1} dx \\ &(\text{for } n \geq 1) \end{aligned} \tag{5.35}$$

$$\begin{aligned} P(\text{success in DiPaQ 1}) = &\sum_{n=1}^{N} P(N_{\underline{T^P}} = n | \text{DiPaQ 1}) \\ &\cdot P(\text{success in DiPaQ 1 } |n) \end{aligned} \tag{5.36}$$

5.2.4 DiPaQ 2

The DiPaQ 2 state is similar to DiPaQ 1, but it always follows one of the DiPaQ states, resulting in a different probability of n pending nodes at τ time into the state, as this depends on the duration of the previous state. This influences the total state time and the state success probability. The total DiPaQ 2 state time, $\underline{T^{D2}}$, is also split into four time segments, see Equation. 5.37.

$$\underline{T^{D2}} = E[y^{D2}] + \tau + T + E[T_{rc}^{D2}] \tag{5.37}$$

$E[y^{D2}]$ is calculated similar to the $E[y^{D1}]$ as shown in Equation. 5.31, Equation. 5.32c, and Equation. 5.33, but with $\underline{T^{D1}}$ instead of $\underline{T^P}$. As DiPaQ 2 can also follow an other DiPaQ 2 state instead of a DiPaQ 1 state (Figure. 5.1), it is assumed for this calculation that $\underline{T^{D1}} \approx \underline{T^{D2}}$.

Similar to the previous states, DiPaQ 2 can end in two ways. To calculate $E[T_{rc}^{D2}]$, the estimate $\underline{T_{\text{est}}^{D2}}$ of $\underline{T^{D2}} - \tau$ is needed. This is calculated as in Equation. 5.34 but with $E[y^{D2}]$ and $E[T_{rc,1}^{D2}|n=2]$ instead. Having found this estimate, $E[T_{rc}^{D2}]$ is calculated as shown in Equation. 5.25, Equation. 5.26, and Equation. 5.27, but with P_0^{D2}, P_1^{D2}, $E[T_{rc,0}^{D2}]$ and $E[T_{rc,1}^{D2}]$ based on $\underline{T_{\text{est}}^{D2}}$. Adding $E[y^{D2}]$, $E[T_{rc}^{D2}]$, τ, and T together as shown in Equation. 5.37 finds the expected DiPaQ 2 state time $\underline{T^{D2}}$.

The DiPaQ 2 success probability is calculated just like DiPaQ 1 as shown in Equation. 5.31, Equation. 5.35, and Equation. 5.36, but with $\underline{T^{D2}}$ instead of $\underline{T^{P}}$. This calculation assumes that at high values of load g when the steady state probability of the DiPaQ 2 state is high, the probably of having followed a DiPaQ 2 state is much higher than a DiPaQ 1 state.

5.3 Steady state probabilities

To calculate the model throughput and success rate the steady state probabilities π^i are needed. Equation. 5.38 shows the system of linear equations resulting from all state transition probabilities (Figure. 5.1). This is solved into the steady state probabilities in terms of $p_{D1,P}$, $p_{D2,D1}$, and $p_{D2,D2}$ as shown in Equation. 5.39. Which can be calculated using function $A(n,t,m)$ found in Equation. 5.23 as shown in Equation. 5.40 .

$$\begin{cases} 1 & = \pi^I + \pi^P + \pi^{D1} + \pi^{D2} \\ \pi^P & = \pi^I \\ \pi^{D1} & = \pi^I p_{D1,P} \\ \pi^{D2} & = \pi^{D1} p_{D2,D1} + \pi^{D2} p_{D2,D2} \end{cases} \tag{5.38}$$

$$\pi^I = \frac{1 - p_{D2,D2}}{p_{D1,P}(p_{D2,D1} - p_{D2,D2} + 1) - 2p_{D2,D2} + 2} \tag{5.39a}$$

$$\pi^P = \frac{1 - p_{D2,D2}}{p_{D1,P}(p_{D2,D1} - p_{D2,D2} + 1) - 2p_{D2,D2} + 2} \tag{5.39b}$$

$$\pi^{D1} = \frac{p_{D1,P}(1 - p_{D2,D2})}{p_{D1,P}(p_{D2,D1} - p_{D2,D2} + 1) - 2p_{D2,D2} + 2} \tag{5.39c}$$

$$\pi^{D2} = \frac{(p_{D1,P})(p_{D2,D1})}{p_{D1,P}(p_{D2,D1} - p_{D2,D2} + 1) - 2p_{D2,D2} + 2} \tag{5.39d}$$

$$p_{D1,P} = 1 - P(\text{no arrivals in } \underline{T^P} - \tau) = 1 - A(0, \underline{T^P} - \tau, 0) \tag{5.40a}$$

$$p_{D2,D1} = 1 - A(0, \underline{T^{D1}} - \tau, 0) \tag{5.40b}$$

$$p_{D2,D2} = 1 - A(0, \underline{T^{D2}} - \tau, 0) \tag{5.40c}$$

5.3.1 Model validation

To validate the model, the scenario described in Section 4.2 is modeled and its output is compared to the measurement. Knowing the locations of the nodes the distances between them are calculated by $d = \sqrt{\Delta x^2 + \Delta y^2}$ where d is the euclidean distance between nodes and Δx, Δy the difference in x and y coordinate. Using Gaussian kernel density estimation the PDF and CDF of distance D is estimated. To find constants k and l (Equation. 5.12) all nodes were placed in a line, and programmed to transmit sequentially. Node-1 was programmed to measure the voltage to which its C_{RF} is charged for each distance.

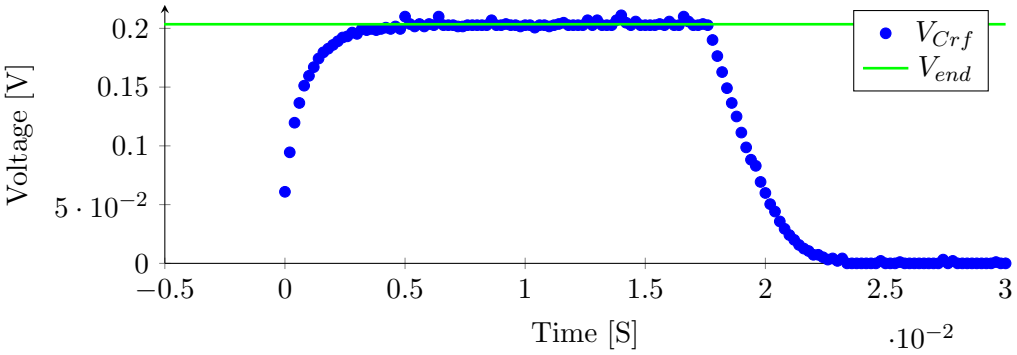

Figure 5.4. Charge in C_{RF} over time, when receiving from a transmitter at 15 cm distance

Figure. 5.4 shows a single C_{RF} measurement at a distance of 15cm between transmitter and receiver from which the maximum charge V_{end} was extracted. Equation. 5.12a was fitted to the voltage over distance data to find the k and l parameter shown in Table 5.2. The threshold voltage in the switch V3.0 was set to 3 mV and the RC value to 0.0050 s. With this information Equation. 5.15 and Equation. 5.16 are used to find the distribution of T_{rc}. A packet size of 100 bytes including preamble results in a packet time of $T = 0.01792$s, and the radio turn-on time normalised to the packet time results in $\tau = 0.0084$. Using the parameters shown in Table 5.2 the expected state times $\underline{T^i}$, state success probabilities $P(\text{success } S_i)$, and steady state probabilities π^i can be calculated for load g as previously shown. Then,

using Equation. 5.1a and Equation. 5.1b we find the model throughput and success rate at load g, the result of which is shown in Figure. 5.5. As seen in the figures, the model success rate and throughput closely follow the measured data. However, when approaching $g = 10^1$ the throughput in the measurement results decreases, while in the model it does not, because a node in the measurement-case cannot have a new packet arrival while it is still transmitting its previous arrival, therefore dropping the packet and reducing its success rate.

Table 5.2
Model parameters to model the scenario described in Section 4.2

Parameter	Value	Parameter	Value
k	-1.146	RC	0.0050 s
l	0.0334	T	0.01792 s
V_{thr}	0.003 V	τ	0.0084

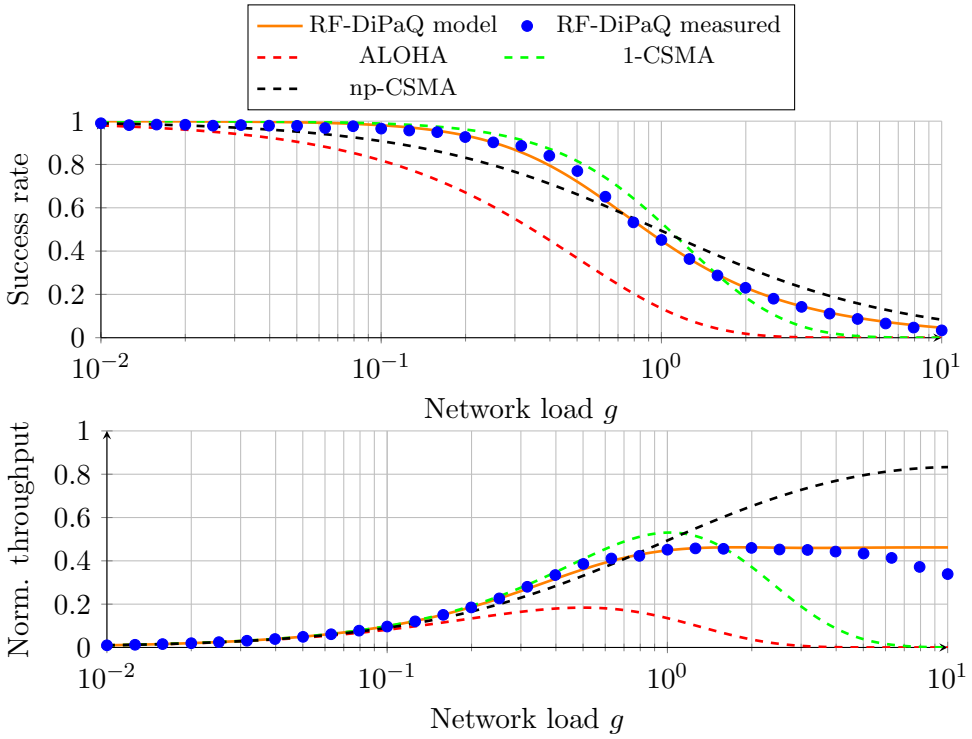

Figure 5.5. Modeled success rate (top) and norm. throughput (bottom) over network load compared to measurement and other protocols

Chapter 6

Hybrid Circuit-Network Simulator

Since the RF-DiPaQ MAC protocol depends heavily on analog circuitry, an analog circuit simulator (Ngspice) was extended with custom network simulation capabilities, which makes it a hybrid circuit-network simulator. This allows us to validate the model and find the limiting conditions of throughput, effect of different topology, and node placements. The advantages are: (1) Since we use standard analog circuit simulator, we can simulate charge/discharge of C_{RF} close to reality. (2) It is not easy to practically repeat different experimental scenarios of a large scale network of event-driven EH nodes, an analog simulator helps in repeatability of the experiments.

Our simulator extends the open-source analog simulator Ngspice, with a custom, python-written, agent-based network simulator, enabling us to simulate both the analog circuitry and network capability of the RF-DiPaQ MAC protocol concurrently. The hybrid simulator is designed to be distributed across multiple Virtual Machines (VM), which can simulate multiple scenarios in parallel. Using a SPICE script the analog circuit of the RF-unit can be loaded into the simulator. When the analog circuit is not known, the relation between input power and DC output voltage can be supplied in the form of Equation. 5.12a.

6.1 Simulation overview

Figure. 6.1 shows a high level system overview of the simulator. The cluster head is configured with a specific hardware setup, node layout and range of arrival rates to be evaluated. The cluster head distributes the configured setup to the cluster nodes and supplies each cluster node with an arrival rate. Each cluster node configures an environment with N nodes based on

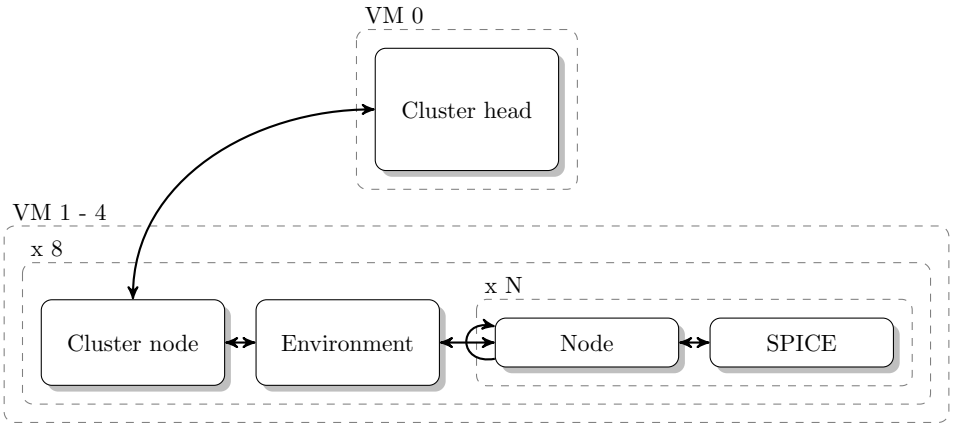

Figure 6.1. High level simulation system overview

the configuration given by the cluster head. Each of the N nodes is in turn configured with the Ngspice reference model or DC output voltage. During the simulation, nodes interact with each other, indicating when each node starts or stops transmitting. Based on the distance to the transmitter(s) and the pathloss model each node calculates an input power and calculates or simulates the voltage level to which its C_{RF} is charged. Based on the voltage across the C_{RF} the network decisions regarding transmissions are taken following the RF-DiPaQ protocol. Figure. 6.2 shows a snapshot of a simulation, revealing the voltage in the C_{RF}s of nine nodes over time along with the color-matched RF activity of each node. Note the similarities to Figure. 3.2.

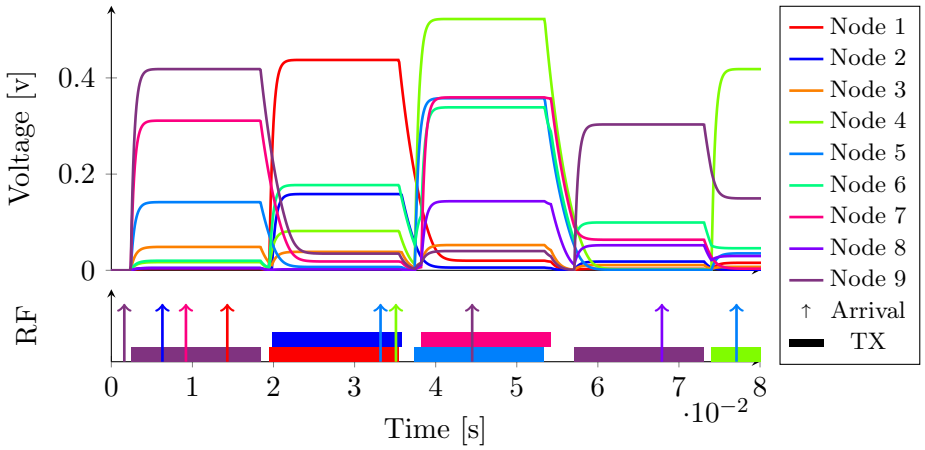

Figure 6.2. Snapshot of a simulation showing the voltages in the reference capacitors C_{RF} of nine nodes reacting to the RF activity over time

6.2 Validation of the simulator

To validate the simulation, the scenario as described in Section 4.2 and shown in Figure. 4.4 was simulated. From the schematic of the RF-unit of the Switch V3.0 as shown in Figure. 4.2, a SPICE script was made, see Listing 6.1. Using the pathloss model the RSSI is estimated and based on a 50 ohm antenna converted into a sine wave input voltage. Every time a node starts or stops transmitting the input voltage is recalculated. Figure. 6.3 shows the simulation success rate and throughput of the simulator compared to the model and measurement. As expected the simulated results match the model and measurement results. Since in the simulation a node can have a new arrival while transmitting, the network can reach a load of $g = 10^1$ without a decrease in throughput.

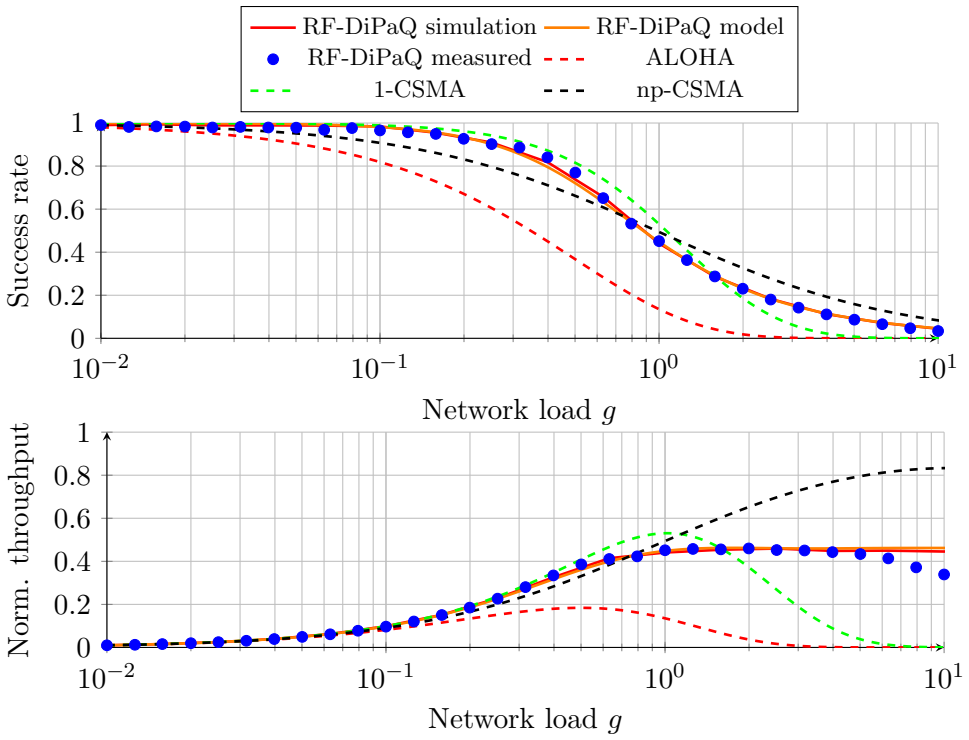

Figure 6.3. Simulated success rate (top) and norm. throughput (bottom) compared to model, measurement, and other protocols

```
.title Switch V3.0 RF-Unit
.include SMS7630.lib
R1 Va V1 50Ω
C1 V1 gnd 16pF
L1 V1 V2 11.1nH
C2 V2 gnd 3.67pF
C3 V2 V3 10pF
XD1 gnd V3 SMS7630
XD2 V3 Vcrf SMS7630
Crf Vcrf gnd 68nF
R2 Vcrf gnd 73.2kΩ
Vinput Va gnd AC SIN(0V 0V 868MEGHz 0s 0Hz)
.save vcrf
.tran [deltaSample]s [simTime]s
.end
```

Listing 6.1: SPICE Switch V3.0 RF-Unit circuit script

Chapter 7

Evaluation

In this section we will evaluate the effect of device-to-device distance on a network of Switch V3.0 nodes. We model and simulate how state-of-the-art WuR front-end hardware would perform if used as RF-unit, show how the optimal RC value can be found, and compare the energy consumption of RF-DiPaQ to the CSMA protocols and classical Aloha.

7.1 Distance between neighboring devices

To test the effect of distance between neighboring devices on the performance of the RF-DiPaQ protocol, nine Switch V3.0 RF-DiPaQ enabled nodes (Figure. 4.1) were placed in a 3 by 3 grid and tested for different grid-neighbor distances, ranging from 25 cm to 150 cm. Figure. 7.1 shows the success rate and the normalised throughput of different grid sizes of 9 nodes. As expected, when using large device-to-device distances (150 cm for the Switch V3.0) the RF-units of the nodes cannot sense the transmissions of other nodes and the performance of the RF-DiPaQ is reduced to the performance of Aloha. This shows how the throughput of RF-DiPaQ degrades when the number of hidden terminals increases. As observed in Figure. 7.1, the shortest grid-neighbor distance does not result in the best performance. 50 cm outperforms 25 cm, because in the 25 cm layout, the reference capacitors C_{RF} of the nodes are charged to relatively higher voltages, resulting in longer average discharge times T_{rc} between two successive transmissions which can not be utilised, reducing the throughput.

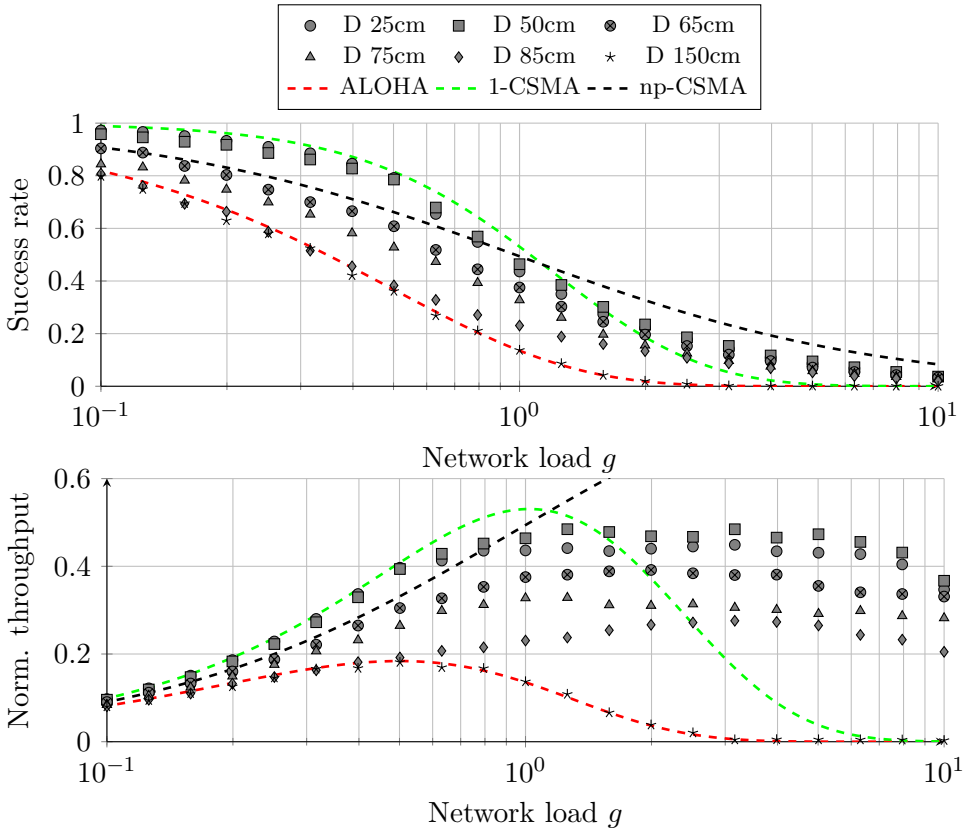

Figure 7.1. Measured success rate (top) and normalised throughput (bottom) of 3 by 3 grid of 9 nodes for different node distances

7.2 WuR-hardware

The performance of RF-DiPaQ depends on the RF-unit efficiency of harvesting the carrier wave and charging the capacitor. As the hardware used in WuR front-ends share many similarities with the RF-unit, they can be repurposed to serve as RF-unit in a RF-DiPaQ scenario. Due to the unavailability of state-of-the-art WuR hardware, the model and simulation can be used to evaluate how WuR hardware would perform while serving as RF-unit. In specific, only the minimal sensitivity and the relation between DC output voltage V_{out} and input power P_{in} are needed. This allows us to model how the microwatt-WuR proposed by DelPrete *et al.* [5] would perform if adapted to serve RF-DiPaQ functionalities. The relation between V_{out} and P_{in}, is given in Equation. 7.1, and holds for $P_{in} \in [-70\,dBm, -35\,dBm]$. The minimal sensitivity of this hardware results in $V_{thr} = 300\,\mu V$ at an input power of -56 dBm.

$$V_{out} = 10^{aP_{in}+b}, \text{ with } a = 0.100993, b = 2.132736 \tag{7.1}$$

Figure. 7.2 shows the performance of RF-DiPaQ regarding model and simulation using 100 nodes. The nodes are positioned into a 10 by 10 node grid layout spread across a 25 m by 25 m area. Prospective use-cases involving EH-device distributions like the above can be seen inside smart factories where tens/hundreds of sensors are positioned in a few square meters and need to transmit information regarding the structural health of machinery [7] or in cases of on-demand transmissions like the ones depicted in Figure. 1.1 (voting, call-crew buttons) [15]. In terms of our grid layout the minimum distance between any two nodes in the network equals 2.78 m, which results in a maximum P_{in} of less than -35 dBm, staying within the P_{in} range.
As most clearly shown in the success rate in Figure. 7.2, the performance of RF-DiPaQ for 100 nodes outperforms np-CSMA and follows the 1-CSMA performance, until an offered load of $g = 0.8$. As seen in the throughput in Figure. 7.2, after $g = 0.8$, RF-DiPaQ outperforms 1-CSMA with a max normalized throughput of 0.64 at the saturation point $g = 2.51$, compared to 0.53 at $g = 1$ for 1-CSMA. The network under RF-DiPaQ can handle 2.46 times more offered load than 1-CSMA and 4.74 times more than Aloha in saturation. RF-DiPaQ achieves a throughput of 1.21 times more than 1-CSMA, while not spending energy sensing, contrary to the continuous sensing in 1-CSMA. Further, RF-DiPaQ performs better than np-CSMA for lower traffic loads, i.e., till saturation. Using the same number of RF-DiPaQ nodes in smaller grids would lead to saturation at even higher values of g. As the probability of collisions depends on the standard deviation of T_{rc} a smaller RC value could be used while maintaining the standard deviation, but reducing the mean. This would reduce the unutilised time between two successive transmissions while maintaining the probability of collisions, thus increasing the saturation point.

This model and simulation is based on the hardware of a -56 dBm WuR [5], as from this hardware the relation between V_{out} and P_{in} became known. There are however more sensitive WuR designs available like the -79.1 dBm sensitive WuR proposed by Mangal *et al.* [22]. However, their relation between V_{out} and P_{in} is not known and therefore cannot be modeled or simulated in networks of RF-DiPaQ nodes. Nevertheless, RF-DiPaQ nodes with a -79.1 dBm RF-unit would result in a significant larger range. As for the RF-DiPaQ MAC protocol no semantic-addressing is needed; just the carrier wave detection, no sensitivity has to be used, in order to decode the wake up call. Thus the hardware of the state-of-the-art WuRs [9, 28, 34, 22] achieve even higher sensitivity when used as RF-units in RF-DiPaQ scenarios.

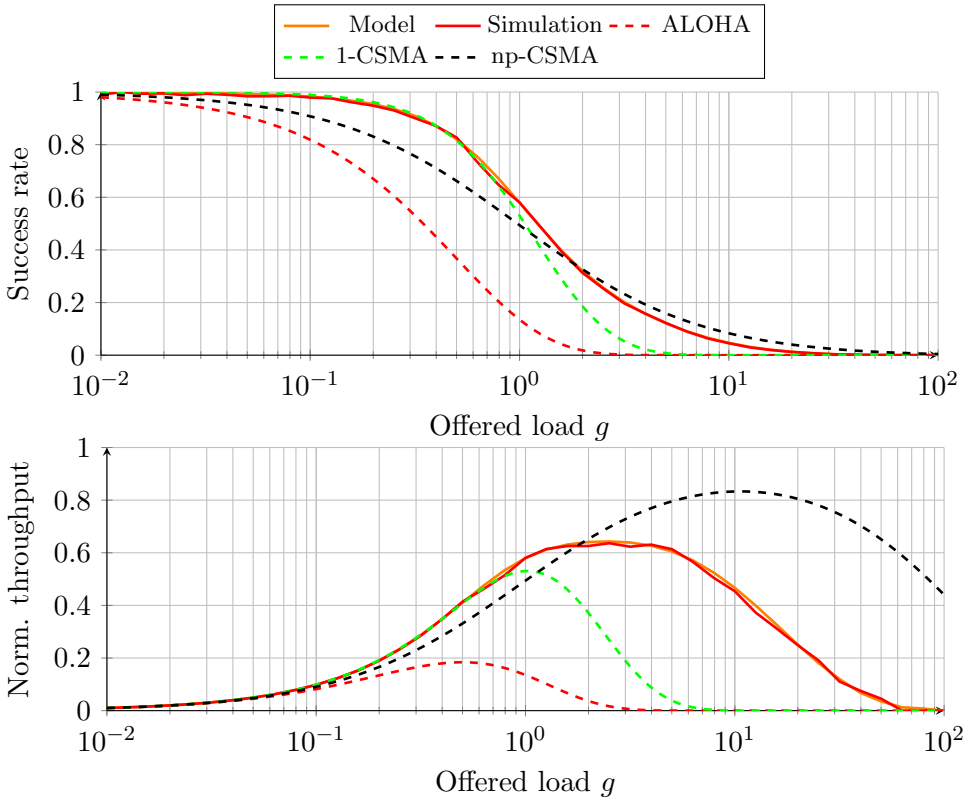

Figure 7.2. Modeled success rate (top) and normalized throughput (bottom) of 100 nodes in grid layout in a 25 m by 25 m area

7.3 Energy consumption

RF-DiPaQ also outperforms 1-CSMA regarding energy usage. In the throughput in Figure. 7.2, when RF-DiPaQ saturates at an offered load of $g = 2.51$, nodes following 1-CSMA spend on average 60% of the packet time T sensing the medium, waiting to transmit. This results in 1.7 times higher energy usage than in RF-DiPaQ. Figure. 7.3 shows the power trace of the Switch V3.0 (Figure. 4.1) while waking up to transmit/channel sensing, showing the power consumption for transmitting and carrier sensing to be 22 mW and 27 mW respectively. For this hardware, the average energy usage per arrival equals 689.5 μJ in 1-CSMA and 410.26 μJ in RF-DiPaQ, as seen in Figure. 7.4. Apart from the above mentioned amount of saved energy which is due to zero energy sensing, RF-DiPaQ also evades collisions by prioritizing transmissions based on distance. These collisions would lead 1-CSMA to consume more energy when having to retransmit. Regarding np-CSMA, energy consumption by sensing depends on how long and how often the medium is sensed (i.e., back-off intervals). Assuming a CCA of

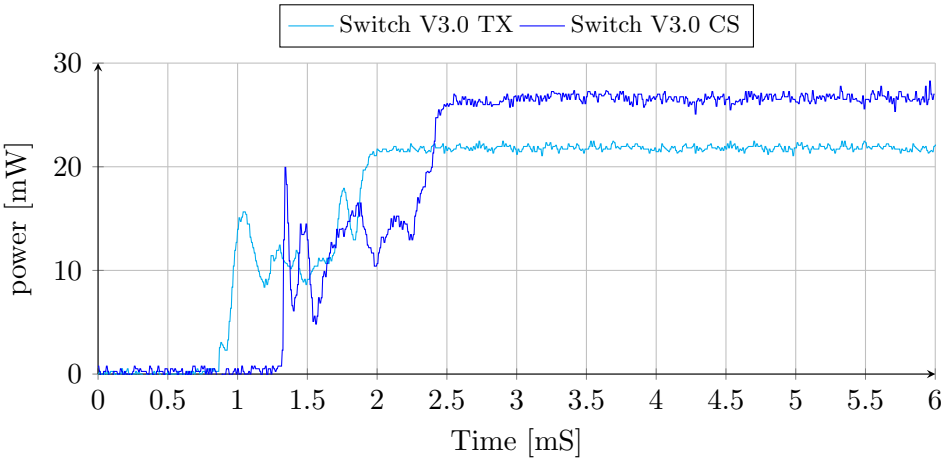

Figure 7.3. Measured power consumption of the Switch V3.0, while waking up from sleep into TX and CS mode

0.15 mS, for the Switch V3.0 this results in a minimum of 20.66 μJ used per assessment. The probability of a packet arriving at a busy medium equals $p = 1/(1+1/g)$. Using the expected value of the geometric distribution, the expected number of failed assessments before transmitting can be calculated to equal $(1/(1-p))-1$. For the Switch V3.0 hardware at an offered load of $g = 2.51$ this results in 2.51 tries before transmitting resulting in an average of 486.72 μJ used per packet, which is still more than the consumed energy per packet of RF-DiPaQ, as seen in Figure. 7.4. As traffic load g increases RF-DiPaQ outperforms the CSMA protocols by a higher factor in terms of energy consumption. At for example $g = 5$, where the throughput of the 100 nodes simulated in Section 7.2 is still above 0.6, 1-CSMA and np-CSMA consume 796.9 μJ and 513.56 μJ respectively while the consumption of RF-DiPaQ stays the same, as shown in Figure. 7.4. When specifically compared to np-CSMA, RF-DiPaQ consumes 36% less energy at offered load $g = 5$, while 10% less at $g = 1.5$. Figure. 7.5 shows the energy consumption per successful packet transmission at each of the different MAC protocol saturation load.

7.3.1 Selection of RC value

To optimise RF-DiPaQ performance the optimal RC value needs to be found. Besides the threshold level and the voltage to which the reference capacitors C_{RF} are charged, the RC value affects the discharge time. A relatively larger RC value results in longer average discharge times. As the discharge time between two successive transmissions cannot be utilised this limits the network throughput. Apart from the average discharge time, the RC value also influences its variance. Lower RC values result in a smaller discharge

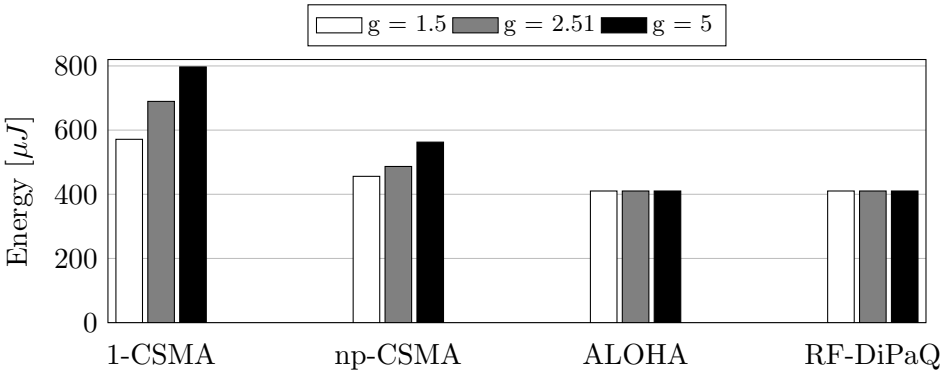

Figure 7.4. Consumed energy per packet transmission for different MAC protocols, for three different offered load values

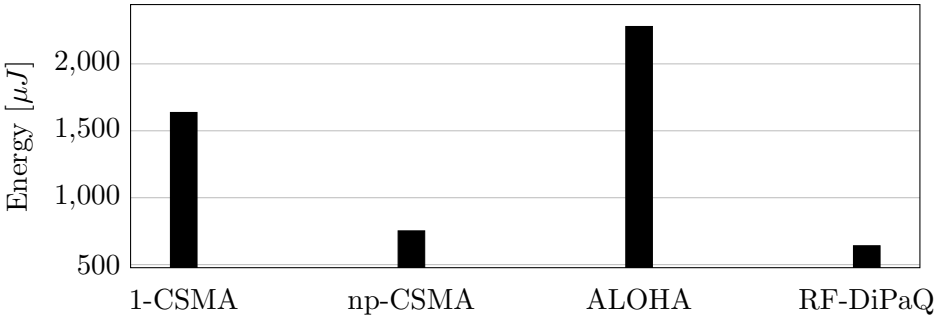

Figure 7.5. Consumed energy per successful packet transmission for different MAC protocols at their saturation load

time variance, increasing the probability of two pending nodes having the same discharge time, causing a collision. However, a lower average discharge time also lowers the probability of an arriving packet finding a busy medium. At low values of offered load g this increases the success rate, making RF-DiPaQ match 1-CSMA as shown in Figure. 7.6 for RC values up to 1ms. The optimal RC value is small enough to not result in overly large average discharge times, and large enough to not result in many collisions. Finding the optimal RC value can be done by modeling a range of different values. Figure. 7.6 presents the success rate and throughput of the Switch V3.0 in the scenario described in Section 4.2 for different RC values and shows how the optimal RC value for the Switch V3.0 was found. As seen in the throughput in Figure. 7.6, the RC value of 0.0050 s results in optimal performance. When the RC value is increased (0.0100 s and 0.0200 s) the maximum throughput is reduced. When the RC value is decreased (0.0010 s and 0.0005 s) the probability of collisions increases, reducing the throughput at higher levels of offered load g.

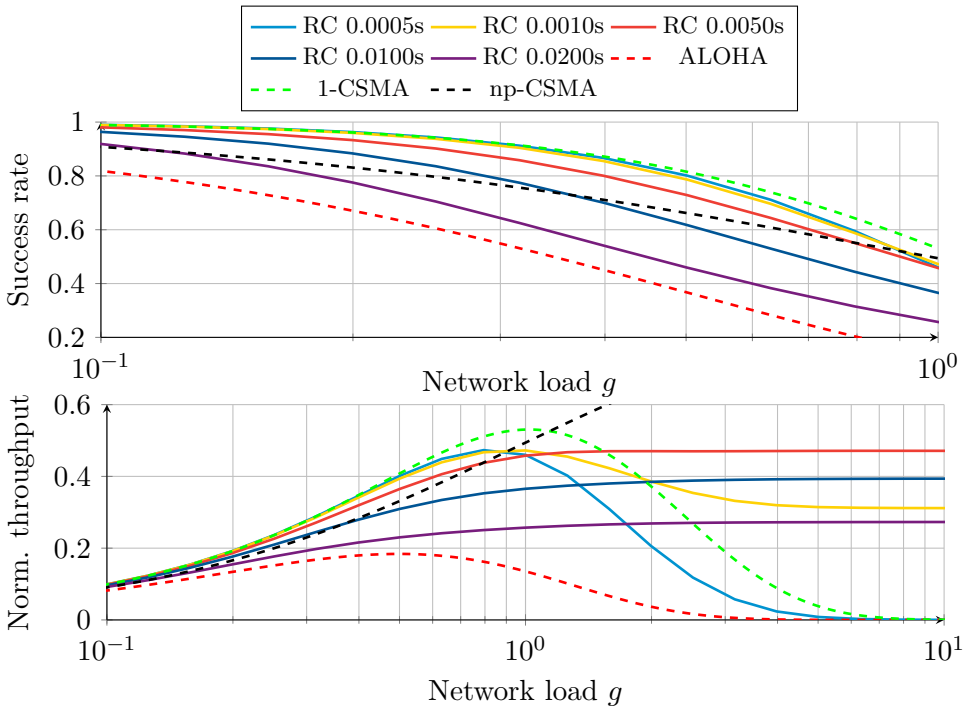

Figure 7.6. Modeled success rate (top) and norm. throughput (bottom) of 9 nodes in a grid layout in a 1m by 1m area for different RC values

Chapter 8

Future work

In this chapter we will talk about the work that could not be done within the time scope of this thesis and is left as future work. We will first talk about how the hardware can be improved upon and will finish with how RF information harvesting can be used outside event-driven energy harvesting schemes.

8.1 hardware

As this thesis has focused on the mechanism behind the RF-DiPaQ MAC protocol, the hardware has not been optimised. As mentioned in Section 7.2 lots of research has been done one wake-up radios which front-end hardware can be re-purposed to serve as RF-unit within the RF-DiPaQ MAC. Although this hardware has been modeled and simulated within the RF-DiPaQ context, actual hardware would allow for large scale tests, i.e. studying RF-DiPaQ in use-case like scenarios.

A hardware optimisation that could be made, is to change the way of discharge of the reference capacitor. Currently the capacitor discharges following an exponential RC discharge curve. One could look into discharging the capacitor using a current mirror to discharge the capacitor at a linear rate. In the current schematic the probability of collision is determent by the ratio of the node capacitor voltages, where in the linear discharge schematic, the absolute difference between the two voltages determines if nodes will collide. This could increase the T_{rc} variance and improve the overall RF-DiPaQ performance.

8.2 RF information harvesting

We have used RF-DiPaQ to introduce the concept of RF-information harvesting, however RF-information harvesting is not limited to event-based energy harvesting schemes. For example the receiver initiated MAC protocol, RIVER-MAC, proposed by Wymore *et al.* [37] uses a CCA-based rendezvous to reduce idle listening for the sender node, and a beacon train-based collision resolution. RF-information harvesting can be used to both perform the CCA-based rendezvous and replace the beacon based collision resolution, reducing the energy consumption of both sender and receiver nodes while also reducing the delay, especially when the offered load increases.

As shown in Figure. 7.4, RF-DiPaQ outperforms 1-CSMA energy-wise by being able to sense the radio medium without the need for an increased energy budget. This is critical in event-based energy harvesting scenarios, where energy is extremely limited. However, RF-DiPaQ can also be applied in other non event-based energy harvesting scenarios to reduce the energy consumption per packet transmission without having to sacrificing the ability of carrier sensing, i.e. reducing the throughput. For example battery powered sensor nodes would see an increase in battery life while maintaining their throughput.

Chapter 9

Conclusion

We considered a class of extreme wireless sensor network, wherein the nodes are batteryless and completely powered by energy harvesting from events such as press of a switch. These nodes are severely energy constrained and cannot have the ability to create and maintain networks and/or coordinate among neighboring nodes resulting in aloha like behavior.

The proposed RF-DiPaQ protocol uses the novel technique of RF information harvesting to sense the medium, and prioritize channel access among devices based on distance from the current transmitter. We detailed the design of RF-DiPaQ nodes, wherein the amount of RF-energy that is harvested charges a reference capacitor, C_{RF}. When C_{RF} is discharged to a threshold V_{thr} the device uses the event-driven harvested energy to transmit. We validated our protocol on-field using Switch V3.0 nodes, modeled RF-DiPaQ, and formulated the relationships over successful transmission probabilities and state-time for each state of our model. We developed a hybrid circuit-network simulator to evaluate in conditions as close to reality as possible. We used the parameters from state-of-the-art wake-up radios for simulation and show RF-DiPAQ performs well, but were hindered to implement on our on-field tests due to the current social circumstances.

The evaluation of RF-DiPaQ against the main contention-based MAC protocols showed that it outperforms 1-CSMA with a max normalized throughput of 0.64 at the saturation point $g = 2.51$, compared to 0.53 at $g = 1$ for 1-CSMA. The network under RF-DiPaQ can handle 2.46 times more offered load than 1-CSMA and 4.74 times more than Aloha in saturation. Furthermore, when compared to np-CSMA, which is the best among p-CSMA, np-CSMA and 1-CSMA for high offered loads, RF-DiPaQ consumes 36% less energy at offered load $g = 5$, while 10% less at $g = 1.5$. Hereby we show how effective medium utilization can be achieved for event driven energy harvesting wireless sensor nodes without increasing energy budget.

Bibliography

[1] D. Altinel and G. Karabulut Kurt. Modeling of multiple energy sources for hybrid energy harvesting iot systems. *IEEE Internet of Things Journal*, 6(6):10846–10854, 2019.

[2] J. M. Amanor-Boadu, M. A. Abouzied, and E. Sánchez-Sinencio. An efficient and fast li-ion battery charging system using energy harvesting or conventional sources. *IEEE Transactions on Industrial Electronics*, 65(9):7383–7394, 2018.

[3] Y. H. Bae and J. W. Baek. Sensing strategy exploiting channel memory in CR network with RF energy harvesting. *IEEE Communications Letters*, 22(12):2539–2542, 2018.

[4] Shun Yan Cheung. Performance Analysis of the unslotted 1-persistent CSMA protocol. `http://www.mathcs.emory.edu/~cheung/Courses/558/Syllabus/00/CSMA/csma-anal1a`. Accessed: 2020-02-18.

[5] M. Del Prete, A. Costanzo, M. Magno, D. Masotti, and L. Benini. Optimum excitations for a dual-band microwatt wake-up radio. *IEEE Transactions on Microwave Theory and Techniques*, 64(12):4731–4739, 2016.

[6] F. Deng, X. Yue, X. Fan, S. Guan, Y. Xu, and J. Chen. Multisource energy harvesting system for a wireless sensor network node in the field environment. *IEEE Internet of Things Journal*, 6(1):918–927, 2019.

[7] ericsson.com. Realizing smart manufacturing through IoT. `https://www.ericsson.com/en/mobility-report/articles/realizing-smart-manufact-iot`. [Online; accessed: 2020-06-07].

[8] Kai Geissdoerfer, Mikołaj Chwalisz, and Marco Zimmerling. Shepherd: A portable testbed for the batteryless iot. In *Proceedings of the 17th Conference on Embedded Networked Sensor Systems*, SenSys '19, page 83–95. Association for Computing Machinery, 2019.

[9] D. Ghose, F. Y. Li, and V. Pla. MAC protocols for wake-up radio: Principles, modeling and performance analysis. *IEEE Transactions on Industrial Informatics*, 14(5):2294–2306, 2018.

[10] T. Ha, J. Kim, and J. Chung. He-mac: Harvest-then-transmit based modified edcf mac protocol for wireless powered sensor networks. *IEEE Transactions on Wireless Communications*, 17(1):3–16, 2018.

[11] D. T. Hoang, D. Niyato, P. Wang, and D. I. Kim. Opportunistic channel access and RF energy harvesting in cognitive radio networks. *IEEE Journal on Selected Areas in Communications*, 32(11):2039–2052, 2014.

[12] Texas Instruments. CC1352R product page. `https://www.ti.com/product/CC1352R#`. Accessed: 2019-05-07.

[13] H. Karvonen, J. Petäjäjärvi, J. Iinatti, M. Hämäläinen, and C. Pomalaza-Ráez. A generic wake-up radio based mac protocol for energy efficient short range communication. In *2014 IEEE 25th Annual International Symposium on Personal, Indoor, and Mobile Radio Communication (PIMRC)*, pages 2173–2177, 2014.

[14] L. Kleinrock and F. Tobagi. Packet switching in radio channels: Part i - carrier sense multiple-access modes and their throughput-delay characteristics. *IEEE Transactions on Communications*, 23(12):1400–1416, 1975.

[15] N. Kouvelas, A. K. Keshava, S. Narayana, and R. V. Prasad. Pushing the boundaries of IoT: Building and testing self-powered batteryless switch. In *2019 IEEE 5th World Forum on Internet of Things (WF-IoT)*, pages 231–236, 2019.

[16] M. Ku, W. Li, Y. Chen, and K. J. Ray Liu. Advances in energy harvesting communications: Past, present, and future challenges. *IEEE Communications Surveys Tutorials*, 18(2):1384–1412, Secondquarter 2016.

[17] J. C. Kwan and A. O. Fapojuwo. Radio frequency energy harvesting and data rate optimization in wireless information and power transfer sensor networks. *IEEE Sensors Journal*, 17(15):4862–4874, 2017.

[18] Trong Nhan Le, Michele Magno, Alain Pegatoquet, Olivier Berder, Olivier Sentieys, and Emanuel Popovici. Ultra low power asynchronous mac protocol using wake-up radio for energy neutral wsn. In *Proceedings of the 1st International Workshop on Energy Neutral Sensing Systems*. Association for Computing Machinery, 2013.

[19] X. Lu, P. Wang, D. Niyato, D. I. Kim, and Z. Han. Wireless networks with RF energy harvesting: A contemporary survey. *IEEE Communications Surveys Tutorials*, 17(2):757–789, 2015.

[20] Brandon Lucia, Vignesh Balaji, Alexei Colin, Kiwan Maeng, and Emily Ruppel. Intermittent computing: Challenges and opportunities. In *2nd Summit on Advances in Programming Languages (SNAPL 2017)*. Schloss Dagstuhl-Leibniz-Zentrum fuer Informatik, 2017.

[21] M. Magno, V. Jelicic, B. Srbinovski, V. Bilas, E. Popovici, and L. Benini. Design, implementation, and performance evaluation of a flexible low-latency nanowatt wake-up radio receiver. *IEEE Transactions on Industrial Informatics*, 12(2):633–644, 2016.

[22] V. Mangal and P. R. Kinget. 28.1 a 0.42nw 434mhz -79.1dbm wake-up receiver with a time-domain integrator. In *2019 IEEE International Solid- State Circuits Conference - (ISSCC)*, pages 438–440, 2019.

[23] J. Moody, A. Dissanayake, H. Bishop, R. Lu, N. Liu, D. Duvvuri, A. Gao, D. Truesdell, N. S. Barker, S. Gong, B. H. Calhoun, and S. M. Bowers. A -106dbm 33nw bit-level duty-cycled tuned rf wake-up receiver. In *2019 Symposium on VLSI Circuits*, pages C86–C87, 2019.

[24] M. Y. Naderi, P. Nintanavongsa, and K. R. Chowdhury. RF-MAC: A medium access control protocol for re-chargeable sensor networks powered by wireless energy harvesting. *IEEE Transactions on Wireless Communications*, 13(7):3926–3937, 2014.

[25] Cuong Van Nguyen, Toan Van Quyen, Anh My Le, Linh Hoang Truong, and Minh Tuan Nguyen. Advanced Hybrid Energy Harvesting Systems for Unmanned Ariel Vehicles (UAVs). *Advances in Science, Technology and Engineering Systems Journal*, 5(1):34–39, 2020.

[26] P. Nintanavongsa, U. Muncuk, D. R. Lewis, and K. R.Chowdhury. Design optimization and implementation for rf energy harvesting circuits. *IEEE Journal on Emerging and Selected Topics in Circuits and Systems*, 2(1):24–33, March 2012.

[27] Joaquim Oller, Ilker Demirkol, Jordi Casademont, Josep Paradells, Gerd Ulrich Gamm, and Leonhard Reindl. Wake-up radio as an energy-efficient alternative to conventional wireless sensor networks mac protocols. In *Proceedings of the 16th ACM International Conference on Modeling, Analysis & Simulation of Wireless and Mobile Systems*, MSWiM '13, page 173–180. Association for Computing Machinery, 2013.

[28] R. Piyare, A. L. Murphy, C. Kiraly, P. Tosato, and D. Brunelli. Ultra low power wake-up radios: A hardware and networking survey. *IEEE Communications Surveys Tutorials*, 19(4):2117–2157, 2017.

[29] R. V. Prasad, S. Devasenapathy, V. S. Rao, and J. Vazifehdan. Reincarnation in the ambiance: Devices and networks with energy harvesting. *IEEE Communications Surveys Tutorials*, 16(1):195–213, 2014.

[30] L. Probst, B. Pedersen, and L. Dakkak-Arnoux. Energy harvesting to power the rise of the Internet of Things. `https://ec.europa.eu/growth/tools-databases/dem/monitor/sites/default/files/DTM_Energy%20harvesting%20v1_0.pdf`. [Online; accessed: 2020-06-24].

[31] J. Ren, J. Hu, D. Zhang, H. Guo, Y. Zhang, and X. Shen. RF energy harvesting and transfer in cognitive radio sensor networks: Opportunities and challenges. *IEEE Communications Magazine*, 56(1):104–110, 2018.

[32] C. Schurgers, V. Tsiatsis, S. Ganeriwal, and M. Srivastava. Optimizing sensor networks in the energy-latency-density design space. *IEEE Transactions on Mobile Computing*, 1(1):70–80, 2002.

[33] Hafiz Husnain Raza Sherazi, Luigi Alfredo Grieco, and Gennaro Boggia. A comprehensive review on energy harvesting mac protocols in wsns: Challenges and tradeoffs. *Ad Hoc Networks*, 71:117 – 134, 2018.

[34] D. Spenza, M. Magno, S. Basagni, L. Benini, M. Paoli, and C. Petrioli. Beyond duty cycling: Wake-up radio with selective awakenings for long-lived wireless sensing systems. In *2015 IEEE Conference on Computer Communications (INFOCOM)*, pages 522–530, 2015.

[35] K. Wiklundh and P. Stenumgaard. Massive IoT and EMC. `https://www.electronic.se/en/2018/12/28/massive-iot-and-emc/`. [Online; accessed: 2020-06-07].

[36] T. Wu, F. Wu, J. Redouté, and M. R. Yuce. An autonomous wireless body area network implementation towards IoT connected healthcare applications. *IEEE Access*, 5:11413–11422, 2017.

[37] M. L. Wymore and D. Qiao. RIVER-MAC: A receiver-initiated asynchronously duty-cycled MAC protocol for the Internet of Things. In *2019 IEEE*

43rd Annual Computer Software and Applications Conference (COMPSAC), volume 1, pages 860–869, 2019.

[38] Z. Yi, B. Yang, W. Zhang, Y. Wu, and J. Liu. Batteryless tire pressure real-time monitoring system driven by an ultralow-frequency piezoelectric rotational energy harvester. *IEEE Transactions on Industrial Electronics*, pages 1–1, 2020.

[39] M. Zgaren and M. Sawan. A high-sensitivity battery-less wake-up receiver for 915 mhz ism band applications. In *2015 IEEE International Conference on Electronics, Circuits, and Systems (ICECS)*, pages 336–339, 2015.